

TUNABLE ENHANCEMENT OF LIGHT-MATTER  
INTERACTION IN GRAPHENE HETEROSTRUCTURES

WYATT WRIGHT

A THESIS  
IN  
THE DEPARTMENT  
OF  
PHYSICS

PRESENTED IN PARTIAL FULFILLMENT OF THE REQUIREMENTS  
FOR THE DEGREE OF MASTER OF SCIENCE (PHYSICS)  
CONCORDIA UNIVERSITY  
MONTRÉAL, QUÉBEC, CANADA

AUGUST 2022

© WYATT WRIGHT, 2022

CONCORDIA UNIVERSITY  
School of Graduate Studies

This is to certify that the thesis prepared

By: **Wyatt Wright**

Entitled: **Tunable Enhancement of Light-matter Interaction in  
Graphene Heterostructures**

and submitted in partial fulfillment of the requirements for the degree of

**Master of Science (Physics)**

complies with the regulations of this University and meets the accepted standards  
with respect to originality and quality.

Signed by the final examining committee:

_____	Valter Zazubovits	Chair
_____	Valter Zazubovits	Examiner
_____	Ingo Salzmänn	Examiner
_____	Alexandre Champagne	Supervisor

Approved \_\_\_\_\_  
Pablo Bianucci, GPD  
Chair of Department or Graduate Program Director

\_\_\_\_\_ 20 \_\_\_\_\_  
Pascale Sicotte  
Dean of Faculty of Arts and Science

# Abstract

## Tunable Enhancement of Light-matter Interaction in Graphene Heterostructures

Wyatt Wright

Optoelectronic applications and the exploration of 2D light-matter interactions often require an increase on the bare light absorption of ultra-thin 2D materials (2DM)s, such as graphene. Light absorption by these 2DMs can be enhanced by their incorporation in planar heterostructures which can act as optical interferometric cavities. Furthermore, by fabricating an optical cavity with a suspended 2DM, we can tune its light absorption by tuning the thickness of the air spacer ( $h_{air}$ ). We report the development of an all-dry deterministic transfer technique that is capable of suspending ultra-thin 2DMs in order to fabricate suspended optical cavities, and also the ability to tune the light absorption of said cavities *in-situ* by the electrostatic tuning of  $h_{air}$ . We studied the absorption of visible light in suspended bilayer graphene (BLG) through Raman spectroscopy, which can distinguish the light scattering and absorption of the graphene layer from the rest of the heterostructure. We first adapted models for the exclusive light absorption and the Raman scattering enhancement (Raman factor) of arbitrary planar 2DM heterostructures using Fresnel equations. In order to fabricate pristine, suspended heterostructures, we developed a transfer method which capitalizes on the softness and adhesion of a nitrocellulose micro-stamp to dry-pickup and deterministically transfer 2DMs. This transfer method proved capable of fabricating on-substrate (95% success) and suspended (93%) optical cavities. Raman measurements on a partially-suspended BLG optical cavity agreed with our Raman factor model and demonstrated our ability to tune Raman factor (3.8x) and light absorption (6.3x) over a cavity thickness varying from 0–150 nm. We then sought to further enhance and tune Raman factor *in-situ* through the addition of an aluminium (Al) back-plane mirror, which can also act as a gate electrode to electrostatically tune  $h_{air}$  for suspended devices. On-substrate BLG optical cavity

devices with an Al back-plane mirror demonstrated that Raman scattering can be tuned by a factor of 19 with cavity thickness differences on the order of 75 nm. We next assembled an optical cavity by suspending BLG over Al, whose Raman measurements at  $V_g = 0$  V demonstrated that Raman factor can be tuned 1.8x over a 10 nm change of  $h_{air}$  in the same device. Once applying a gate voltage, our final measurements demonstrated an ability to electrostatically tune Raman factor by  $\approx 20\%$  and  $h_{air}$  by  $\approx 3$  nm with the application of 500 mV. These results pave the way for further research into the *in-situ* tunability of light-matter interactions for enhanced light absorption at higher gate voltages.

# Acknowledgments

Late again. What can I say, I'm an old dog. Completing this degree has been my hardest challenge to date. While I'm glad to have finally reached the end of my research career, it remains bittersweet. I would not be in this position if not for the love and support of my family, friends and colleagues, many of whom deserve more than the words to follow:

Thank you to my supervisor, Alex. I would not be where I am today without your guidance and support. I remain amazed by your passion for physics and the patience which you afforded me. Thank you Israel. This is as much your thesis as it is mine. I could not repay in five years what you have given me in two. Best of luck on your journey to a PhD. Thank you to my former labmates, Gareth and Matthew, for your help over the course of my time in the Champagne group. Thank you to my current labmates, Linxiang, Lorena and Amin, for listening to my nonsense. Best of luck in your careers. Thank you to my parents, who supported me every step of the way, even though they had no clue what I was doing. Thank you to my brother, Dylan, and my friends, Casey, Lee, Ian, Jamie, Stew, Josh and Wayne. You're only as good as the company you keep. Most of all, thank you Tehya. Your love and support were essential in getting through the past three years and I owe you everything that I have. Your work ethic never quite rubbed off on me but we both got it done nonetheless. I can't wait to see where we go from here.

# Contents

<b>List of Figures</b>	<b>viii</b>
<b>1 Introduction: Light-matter Interaction in Graphene Optical Cavities</b>	<b>1</b>
1.1 Light absorption in graphene . . . . .	2
1.2 Graphene optical cavities . . . . .	6
1.3 Graphene Raman scattering . . . . .	7
1.4 Modeling exclusive light absorption and Raman factor in graphene heterostructures . . . . .	8
1.4.1 Modeling exclusive light absorption . . . . .	10
1.4.2 Modeling Raman factor . . . . .	12
1.5 Thesis organization . . . . .	14
<b>2 Fabrication of Bilayer Graphene Optical Cavities by Nitrocellulose Micro-stamp Transfer</b>	<b>16</b>
2.1 Mechanical exfoliation of 2D materials . . . . .	17
2.2 Nitrocellulose-based micro-stamp transfer method . . . . .	20
2.2.1 Stamping apparatus . . . . .	21
2.2.2 Nitrocellulose micro-stamp preparation . . . . .	21
2.2.3 Making contact and pick up of naked 2D crystal . . . . .	22
2.2.4 Alignment of 2DM with target substrate . . . . .	23
2.2.5 Release of naked 2D crystal by dissolution of micro-stamp . . . . .	24
2.2.6 Supported and suspended 2D material heterostructures . . . . .	25
2.3 Determining the Raman factor of graphene from experimental data . . . . .	28
2.3.1 Modelling the Raman factors of graphene on silicon dioxide . . . . .	28
2.3.2 Extracting an experimental Raman factor . . . . .	28
2.4 Assigning Raman factors to experimental data and agreement with our model . . . . .	30

<b>3</b>	<b>Enhancement of Graphene Light-matter Interactions in a BLG/air/Al Optical Cavity</b>	<b>33</b>
3.1	Enhancing Raman factor in BLG/hBN/Al optical cavities . . . . .	34
3.2	Fabrication of BLG/air/Al optical cavities and instrumentation for Raman measurements . . . . .	36
3.2.1	Deposition of aluminium mirror and top electrode for in-situ electrostatic tuning . . . . .	36
3.2.2	Suspending bilayer graphene over the aluminium mirror . . . . .	37
3.2.3	Opto-electronic measurement instrumentation . . . . .	38
3.3	Measurement of Raman factor for a BLG/air/Al optical cavity . . . . .	40
3.3.1	Reducing spatial uncertainty due to microscope stage drift . . . . .	40
3.3.2	Raman signal from microfabrication residues . . . . .	41
3.4	Experimental Raman factor vs theoretical model . . . . .	43
3.5	Gate voltage tunability of light-matter interactions in graphene . . . . .	46
3.5.1	Tuning optical cavity thickness with $V_g$ . . . . .	48
3.5.2	Tuning Raman factor <i>in-situ</i> with $V_g$ . . . . .	50
3.5.3	Device packaging and instrumentation for electro-optical measurements . . . . .	52
3.5.4	Measurement of Raman factor vs gate voltage . . . . .	54
<b>4</b>	<b>Conclusions and Outlook</b>	<b>56</b>
4.1	Main results . . . . .	56
4.2	Outlook . . . . .	57
	<b>Bibliography</b>	<b>62</b>

# List of Figures

1.1	Electrostatically tunable optical cavity . . . . .	2
1.2	Graphene lattice and dispersion relation . . . . .	3
1.3	Graphene light absorption . . . . .	4
1.4	Light absorption by single and bilayer graphene . . . . .	5
1.5	Graphene optical cavity . . . . .	6
1.6	Raman light scattering in graphene . . . . .	8
1.7	Raman spectrum of single-layer graphene . . . . .	9
1.8	Optical cavity circulation and interferences . . . . .	11
1.9	Effect of Raman scattering on interferences . . . . .	12
1.10	Exclusive light absorption and Raman factor of BLG heterostructures	14
2.1	Exfoliation and characterization of BLG . . . . .	18
2.2	Characterization of hBN cavity . . . . .	20
2.3	Step-by-step assembly of suspended graphene heterostructure . . . . .	21
2.4	Stamping apparatus . . . . .	22
2.5	Nitrocellulose micro-stamp preparation . . . . .	23
2.6	Pick up of naked 2D materials . . . . .	24
2.7	Alignment of 2DM with a target substrate . . . . .	24
2.8	Dissolution of the nitrocellulose micro-stamp . . . . .	25
2.9	2DM heterostructures . . . . .	26
2.10	On-substrate heterostructures . . . . .	27
2.11	Raman factor of bilayer graphene on a SiO <sub>2</sub> /Si substrate . . . . .	29
2.12	Fitting curves to Raman data . . . . .	30
2.13	Raman factor calibration . . . . .	31
2.14	Experimental agreement with Raman factor model . . . . .	32
3.1	Comparing Si and Al as backplane mirrors in an optical cavity . . . . .	35
3.2	Tunable Raman factor for BLG supported over Al . . . . .	36
3.3	Photolithography and deposition of aluminium electrodes . . . . .	37

3.4	Suspension of bilayer graphene over aluminium . . . . .	38
3.5	Opto-electronic instrumentation to study light-matter interactions . . . . .	39
3.6	Scanning axes for Raman data on Device WWA12 . . . . .	41
3.7	Comparison of length scales . . . . .	42
3.8	Reducing spatial uncertainty due to drift in the z-direction . . . . .	43
3.9	Eliminating spurious Raman counts due to fabrication residue . . . . .	44
3.10	Cavity height and Raman factor model for Device WWA12 . . . . .	45
3.11	Raman factor data for the X direction of Device WWA12 . . . . .	47
3.12	Raman factor data for the Y direction of Device WWA12 . . . . .	48
3.13	Electrostatic deflection of a suspended graphene crystal . . . . .	49
3.14	Modelling graphene deflection with different capacitor geometries . . . . .	51
3.15	Calculated Raman factor as a function of $V_g$ . . . . .	52
3.16	Preparing the optical cavities for opto-electronic measurements . . . . .	53
3.17	Electro-optical instrumentation . . . . .	54
3.18	Raman factor data for Device WWA12 vs $V_g$ . . . . .	55
4.1	Tuning of BLG Raman scattering intensity and exclusive light absorption in suspended optical cavities . . . . .	58
4.2	<i>In-situ</i> gate tunability of Raman scattering intensity . . . . .	59
4.3	Fabrication of hBN trenches for beam-shaped optical cavities . . . . .	60
4.4	Application of tunable light absorption: optical transducer . . . . .	61

# Chapter 1

## Introduction: Light-matter Interaction in Graphene Optical Cavities

Nano-opto-electromechanical systems (NOEMS) combine interactions between optics, electronics and mechanics [1–3]. Recent advances in the ability to transfer, align and stack 2D materials (2DM)s [4, 5] in order to fabricate pristine heterostructures [6, 7] have accelerated experiments in quantum electron transport [8–10] and optoelectronics [11, 12]. Incorporating suspended 2DMs in such heterostructures (as seen in Fig. 1.1) would unlock extensive control of mechanics, as well as its interactions with optics and electronics [1, 2]. For example, vacuum layers offer a uniquely different index of refraction to optimize exciton binding energy and lifetime in 2DM's [13]. A properly designed suspension in the study of quantum transport in twisted bilayer 2DMs (twistronics) [14] would permit the decoupling of the mechanically sensitive bilayers from the strain of the substrate to strain-engineer [15, 16] their quantum phases [17, 18]. Moreover, stacking 2DMs to form optical cavities [19–21] can enhance light-matter interactions enough to hybridize photonics with NEMS physics [8, 13, 22–24].

In this thesis, we present a platform capable of tuning *in-situ* the light-matter interactions - exclusive light absorption and Raman scattering intensity - of 2DMs that have been integrated into optical cavities. Our tunable optical cavity design, presented in Fig. 1.1, consists of suspending bilayer graphene (BLG) over a hexagonal

boron nitride (hBN) trench and above an aluminium mirror (Al). The mechanical freedom afforded by the suspension would allow for the optical cavity height to be tuned by applying an electrostatic force via the Al. The BLG was suspended using our recently developed deterministic transfer method [25] and the cavity height later determined by quantitative agreement between Raman scattering intensity measurements and our Raman factor calculations [26].

This first chapter presents the background necessary for the reader to understand the light absorption and Raman scattering processes in graphene. Then, we present our models for these light-matter interactions in multiple-media heterostructures based on basic Fresnel principles.

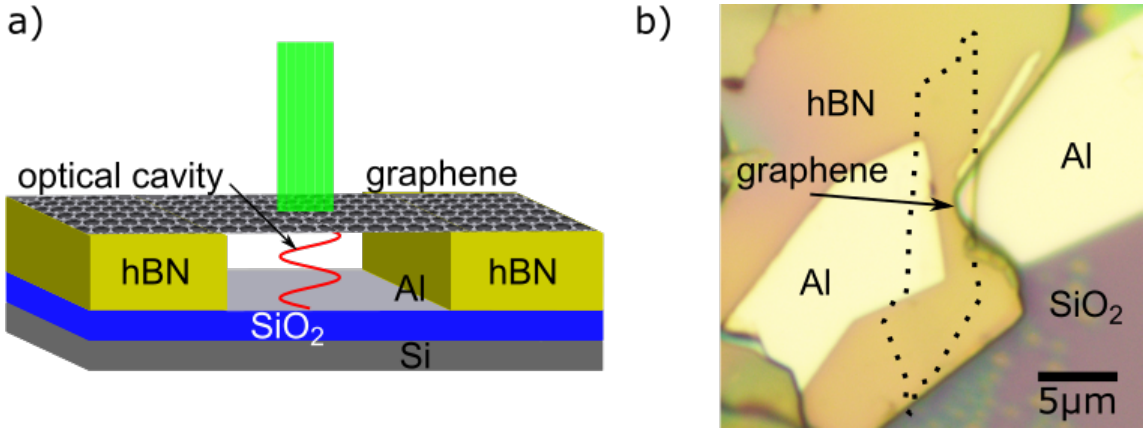


Figure 1.1: Electrostatically tunable optical cavity. (a) Schematic diagram of a tunable optical cavity, where graphene has been suspended above an aluminium electrode. (b) Optical image of a tunable optical cavity. The graphene was transferred to an hBN trench, which resides on a SiO<sub>2</sub>/Si substrate, using a nitrocellulose-based stamping method.

## 1.1 Light absorption in graphene

Graphene is well known for its mechanical, electronic and optical properties due to its peculiar band structure. A single layer of graphene is formed by carbon atoms arranged in a hexagonal lattice with a two-atom basis and interatomic distance of  $a = 1.42 \text{ \AA}$ , as seen in Fig. 1.2(a). In momentum space, the first Brillouin zone possesses two important points,  $K$  and  $K'$ , known as the Dirac points, shown in Fig. 1.2(b). Using a tight-binding model, the electronic dispersion near the  $K$  and  $K'$

points (Fig. 1.2(c)) has a linear relationship of the form [27]:

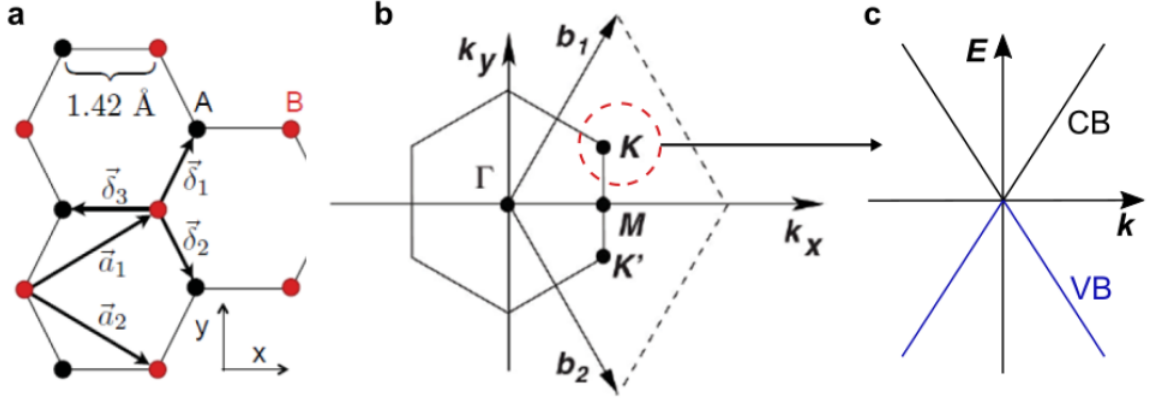


Figure 1.2: Graphene lattice and dispersion relation. (a) Real space hexagonal lattice of graphene, showing two atom basis (A,B), primitive lattice vectors  $\vec{a}_n$ , and nearest neighbour vectors  $\vec{\delta}_n$ . (b) First Brillouin zone of graphene, showing K and K' points at the corners and reciprocal lattice vectors  $\vec{b}_n$ . (c) Low-energy linear graphene dispersion centered at the  $\vec{k} = \vec{K}$  point. Figure reproduced from [26].

$$\hat{H}_{K'}(\vec{k}) = \hbar v_F \vec{\sigma}^* \cdot \vec{k} \quad (1.1)$$

reminiscent of the Dirac-Weyl equation (hence Dirac points).

Light absorption in any material can be traced to the Beer-Lambert law, which describes the intensity of light as it travels through a medium:

$$I(z) = I_0 e^{-\alpha_{abs}(\omega)z} \quad (1.2)$$

where  $\alpha_{abs}(\omega)$  is the absorption coefficient, dependant on the photon's frequency, and  $I_0$  is the incident intensity of light. The absorption coefficient is related to the transmitting material's complex index of refraction,

$$\tilde{n} = n(\omega) + i\kappa(\omega) \quad (1.3)$$

where  $n(\omega)$ , the real part, conserves energy and  $\kappa(\omega)$ , the imaginary part, absorbs energy. The absorption coefficient can be expressed as:

$$\alpha_{abs}(\omega) = \frac{2\omega\kappa(\omega)}{c_0} \quad (1.4)$$

where  $c_0$  is the speed of light in vacuum. The complex index of refraction is also related to the material's dielectric constant [28]:

$$\tilde{n}^2(\omega) = \epsilon(\omega) = 1 + \frac{4\pi i \sigma(\omega)}{\omega} \quad (1.5)$$

where  $\sigma(\omega)$  is the material's conductivity. This conductivity is the sum of intraband and interband contributions. The intraband contributions come from electronic conduction by free carriers in conducting materials, such as metals, and depend on the photon's energy, giving rise to the complex Drude conductivity,  $\sigma_D$ . Interband contributions come from photo-excited electrons who transition from the valence band to the conduction band. Since there is no band gap at the Dirac ( $K, K'$ ) points, the transition rate is determined by Fermi's Golden Rule [28]. The interband conductivity is found to be  $\sigma_i = e^2/4\hbar$ , which is 4 quanta of conductance, without any dependence on the photon's energy [29]. However, interband processes dominate in the visible range of light (shown in Fig. 1.3) and the complex index of refraction can be expressed as:

$$\tilde{n}(\omega) = \sqrt{\epsilon(\omega)} = \sqrt{1 + \frac{4\pi i}{\omega} \sigma_i} \quad (1.6)$$

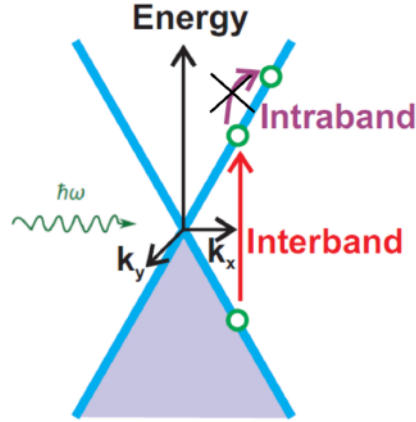


Figure 1.3: Schematic band structure of undoped ( $\mu_F = 0$ ) graphene near the Dirac point. Only interband contributions are possible in the visible range of light. Figure modified from [30].

Since  $\sigma_i \ll \omega$  we can expand the square root to get  $\kappa$ , the imaginary part of our index of refraction. We can now express our absorption coefficient as:

$$\alpha_{abs}(\omega) = \frac{2\omega\kappa}{c_0} \approx \frac{4\pi\sigma_i}{c_0} \approx \frac{\pi e^2}{\hbar c_0} \approx \pi\alpha \quad (1.7)$$

where  $\alpha = e^2/\hbar c_0$  is the fine structure constant. For a single layer of graphene in vacuum, absorption can be approximated as:

$$A_{SLG} = 1 - T_{SLG} - R_{SLG} \approx 1 - e^{-\pi\alpha} \approx \pi\alpha \approx 2.3\% \quad (1.8)$$

meaning that, in this geometry, 2.3% of incident photons are absorbed by the graphene. This absorption was confirmed experimentally, as seen in Fig. 1.4, and is linear up to a few layers, as well as being relatively constant over the visible range of light [29]. Considering its one-atom thickness, graphene has strong light absorption, however this number can be increased further when graphene is incorporated in an optical cavity.

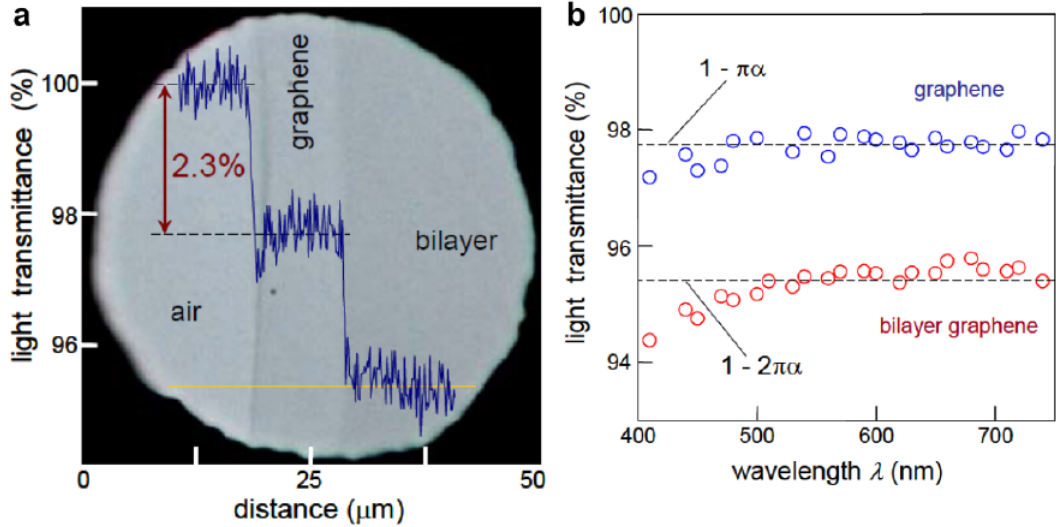


Figure 1.4: Light transmittance in single and bilayer graphene. (a) Optical photograph of a metal ring partially covered with SLG and BLG. The line scan shows white light transmittance along the yellow line, seen near the bottom of the image. (b) Transmittance spectra of the SLG and BLG regions, showing that absorption is near constant over the visible range of light. Figure reproduced from [29].

## 1.2 Graphene optical cavities

Through the enhancement of light absorption by graphene, we could optimize its potential for light harvesting applications [31] and create new tools for NOEMS research [2]. The incorporation of graphene into precisely assembled optical cavities is one mean of achieving this.

Optical cavities are arrangements of spacers (in our case air,  $\text{SiO}_2$ , or hBN) and mirrors (Si or Al) which can trap light, as seen in Fig. 1.5, reflecting it multiple times between the mirror surfaces to produce standing waves for certain frequencies of incident light: frequencies leading to constructive interference are sustained, while those leading to destructive interference are suppressed. For our purposes, an optical cavity represents a photon "recycler", where sustained standing waves lead to additional opportunities for photons to interact with the graphene and be absorbed.

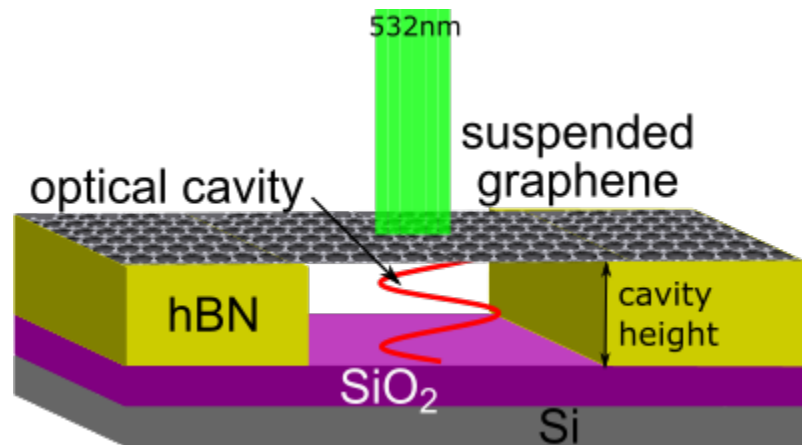


Figure 1.5: Schematic diagram of a graphene optical cavity. Light transmit through the graphene enters the cavity and can be reflected by the substrate, creating an additional chance(s) of being absorbed by the graphene. Interference effects must also be considered, with the nature of the interference (constructive/destructive) being a function of the cavity height.

There are certain aspects to consider when designing one of these cavities. Firstly, the cavity region must have an area which is greater than the area of the excitation laser ( $\geq 1 \mu\text{m}^2$ ). This is to ensure that all of the laser power (photons) is entering the cavity and not the surrounding media. Secondly, the cavity height must be of the same order as the excitation wavelength ( $\lambda = 532 \text{ nm}$ ). A cavity height much greater than the excitation wavelength, would accentuate even slight differences in phase, leading to decreased absorption. Thirdly, if we wish to access the mechanical properties of

the graphene then it must be suspended. While materials such as hBN and SiO<sub>2</sub> are capable of acting as optical cavity spacers, air allows for the freedom to tune the cavity height *in-situ*, opening the possibility of tunable absorption. Hexagonal boron nitride is an ideal building block from which we can suspend graphene since it also possesses a 2D hexagonal crystal lattice, allowing for the graphene to adhere and lay as flat as possible on its surface.

While we have touched on the light absorption by graphene and our optical cavity design, we must also consider the inelastic Raman scattering of light which can occur [32, 33].

### 1.3 Graphene Raman scattering

While our primary interest is enhancing graphene’s exclusive light absorption by fabricating optical cavities, the cavity design presented in the previous section, as well as other experimental factors (such as the presence of a chip carrier when adding electronics), do not allow for transmission measurements typically associated with absorption. In this case, we use reflection measurements, such as Raman spectroscopy, to indirectly measure light absorption.

Raman spectroscopy involves the scattering of incident light inside a given material and then recording the shifted wavelength of the returning photons. The wavelength shifts seen in Raman spectra are unique for every material and serve as a fingerprint of the materials under observation. Although multiple materials are used in our cavity design, the scattering due exclusively to graphene can be resolved [32, 34, 35]. Raman spectroscopy is used to determine the number and orientation of layers, the quality and types of edges, and the effects of perturbations, such as electric and magnetic fields, strain, doping, disorder and defect density [33, 36, 37].

Raman light scattering by graphene occurs when an incident photon ( $\hbar\omega_L$ ) excites an electron-hole pair, as seen in Fig. 1.6. In the transition to the conduction band, a single phonon (G band) or a combination of phonons (2D band) is produced with energy  $\hbar\Omega$ . The electron and hole then recombine and emit a Raman-scattered photon at the shifted frequency,  $\omega_S$ . Conservation of energy ensures that the incident energy is equal to the sum of the scattered phonon and returning photon energies [28, 38].

The Raman spectrum of pristine single-layer graphene (SLG) is shown in Fig.

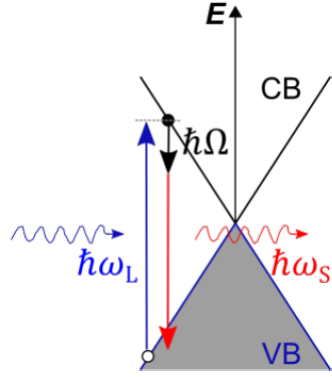


Figure 1.6: Raman light scattering in graphene. An incident photon with frequency  $\omega_L$  excites an electron from the valence to the conduction band. In its transition, the photo-excited electron produces a phonon with frequency  $\Omega$ . The electron and hole then recombine and emit a Raman scattered photon with frequency  $\omega_S$ . Figure modified from [26].

1.7(a) and features two prominent peaks: the G peak and the 2D peak. The G peak occurs around  $1580 \text{ cm}^{-1}$  and is associated with the longitudinal optical (LO) phonon mode, while the 2D peak occurs around  $2700 \text{ cm}^{-1}$  and involves multiple phonons, as seen in Fig. 1.7(c,d). Generally the smallest peak, the D peak (Fig. 1.7(b)), occurs around  $1340 \text{ cm}^{-1}$  and is related to defects in the lattice such as missing carbon atoms or additional impurities [36].

With the background of light absorption and Raman scattering in graphene presented, we now present the models which we adapted in order to analyse our Raman data, as well as direct our optical cavity design.

## 1.4 Modeling exclusive light absorption and Raman factor in graphene heterostructures

Since only a tiny fraction of photons undergo Raman scattering, light absorption is linearly proportional to Raman scattering intensity in an isolated 2D crystal [33]. It has been shown that both the light absorption and Raman scattering intensity can be enhanced in planar heterostructures via constructive and destructive interferences at the interfaces between their constituent layers [39]. Here we develop a quantitative model based on Fresnel equations for the exclusive light absorption,  $A$ , and Raman

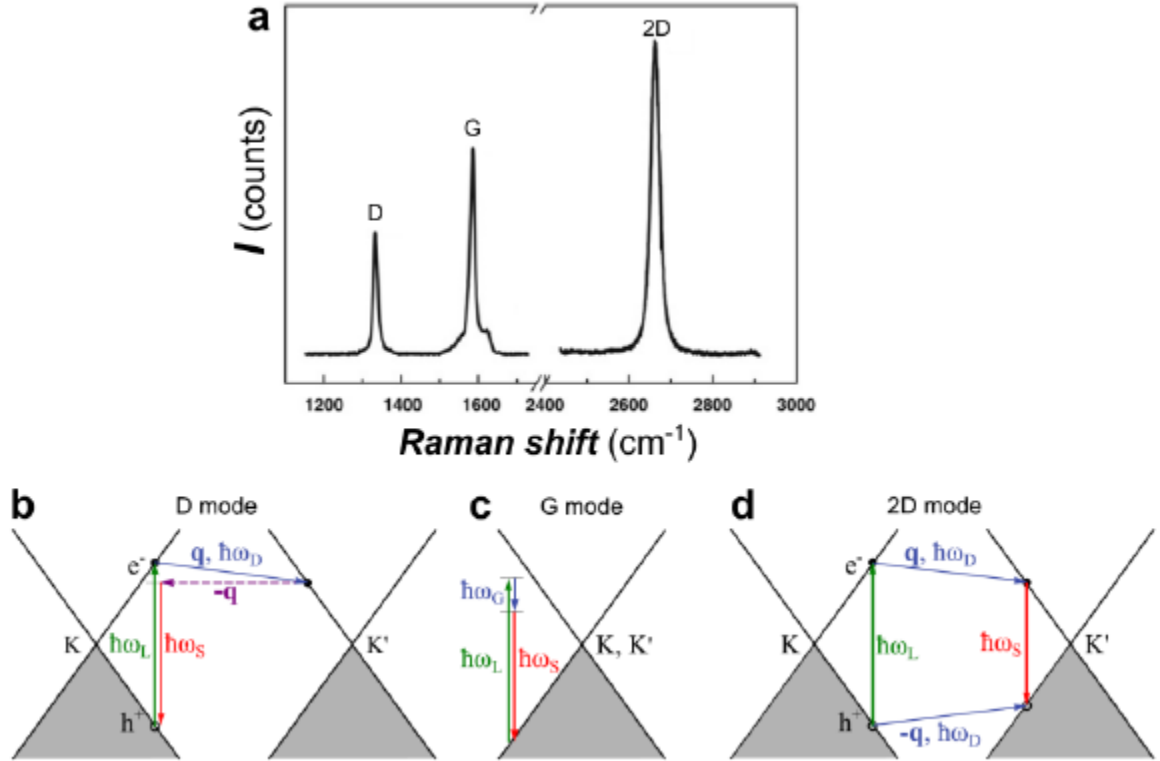


Figure 1.7: Raman spectrum of SLG. (a) Raman spectrum featuring SLG's three prominent peaks: the defect-induced D peak, and the first order and second order G and 2D peaks, respectively. (b-d) Schematics of the three Raman peaks.  $\omega_L$  ( $\omega_S$ ) denote the incoming laser (Raman scattered) photon frequencies. (b) The D peak involves single electron-phonon (solid arrow) and electron-defect (dashed arrow) scattering processes. (d) The 2D peak involves two phonons with frequency  $\omega_D$  and momenta  $\pm q$ . Figure reproduced from [36].

factor,  $F$ , of graphene heterostructures.

### 1.4.1 Modeling exclusive light absorption

The optical cavities which we fabricate are heterostructures with multiple layers. The interfaces between each layer, as well as layer spacing (Fig. 1.8(a)), both contribute to interferences which can lead to increased/decreased light absorption by the graphene.

When light strikes the interface between two media, with indices of refraction  $\tilde{n}_i$  for the first and  $\tilde{n}_j$  for the second, both reflection and refraction may occur. Fresnel coefficients for reflection,  $\tilde{r}_{i,j}$ , and transmission,  $\tilde{t}_{i,j}$ , produce the ratios of the respective reflected and transmitted electric fields to the incident electric field for both p (E-field parallel to incident plane) and s-polarized (E-field perpendicular to the incident plane) [40]:

$$\tilde{t}_{i,j} = \frac{2\tilde{n}_i}{\tilde{n}_i + \tilde{n}_j} \quad (1.9a)$$

$$\tilde{r}_{i,j} = \frac{\tilde{n}_i - \tilde{n}_j}{\tilde{n}_i + \tilde{n}_j} \quad (1.9b)$$

These equations assume that the interface between the media is flat and that the media, themselves, are both homogeneous and isotropic. The light is also assumed to be a plane wave (any incident light field can be decomposed into plane waves and polarizations) that is normally incident on the interface. (It must be noted that the devices presented in this thesis have tilt angles on the order of  $1 - 3^\circ$  (ex: 150 nm change in height over 3  $\mu\text{m}$ ) and we estimate a maximum incidence of  $5^\circ$  from our laser (0.4 mm beam radius with a working distance of 4.5 mm). We plan on adding angle of incidence to our model in the near future.) Since these are complex ratios they not only describe relative amplitudes, but also the phase shift produced by the interface:

$$\tilde{\beta}_i = k\tilde{n}_i h_i = \frac{2\pi}{\lambda} \tilde{n}_i h_i \quad (1.10)$$

where  $h_i$  is the thickness of the medium and  $\lambda$  is the incident wavelength.

Fresnel coefficients for a three-media system are found to be (Fig. 1.8(b)):

$$\tilde{r}_3 = \frac{\tilde{r}_{01} + \tilde{r}_{12}e^{2i\beta_1}}{1 + \tilde{r}_{01}\tilde{r}_{12}e^{2i\beta_1}} \quad (1.11a)$$

$$\tilde{t}_3 = \frac{\tilde{t}_{01}\tilde{t}_{12}e^{i\beta_1}}{1 + \tilde{r}_{01}\tilde{r}_{12}e^{2i\beta_1}} \quad (1.11b)$$

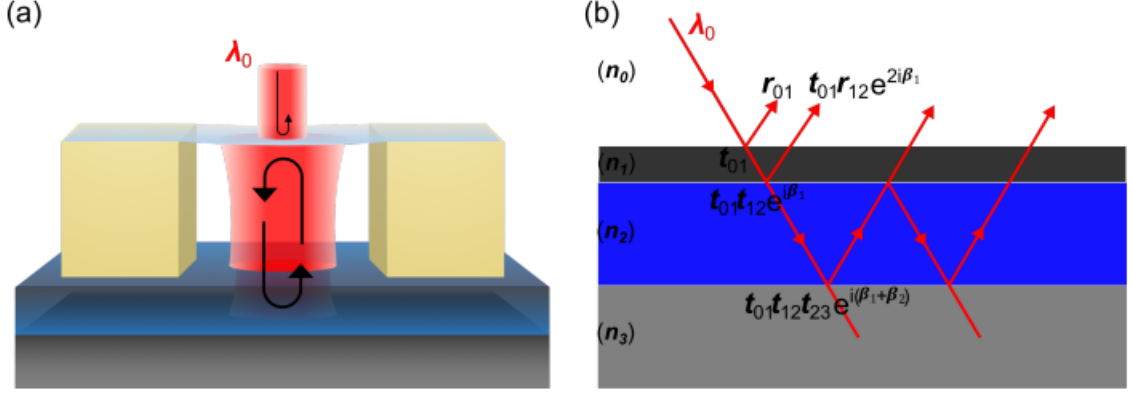


Figure 1.8: Suspended 2DM optical cavity and optical interferences leading to absorption. (a) Schematic of the enhanced circulating power inside an optical cavity due to mirror spacing. (b) Schematic of Fresnel reflections,  $r_{i,j}$ , and transmissions,  $t_{i,j}$ , at the interfaces between media  $i$  and  $j$ . Figure reproduced from [25]

which are found using a recursive method [19]:

$$\tilde{r}_N = \frac{\tilde{r}_{01} + \tilde{r}_{N-1}e^{2i\beta_1}}{1 + \tilde{r}_{01}\tilde{r}_{N-1}e^{2i\beta_1}} \quad (1.12a)$$

$$\tilde{t}_N = \frac{\tilde{t}_{01}\tilde{t}_{12}e^{i\beta_1}}{1 + \tilde{r}_{01}\tilde{r}_{N-1}e^{2i\beta_1}} \quad (1.12b)$$

Total reflection and transmission are defined in terms of the incident ( $P_i$ ), reflected ( $P_r$ ) and transmitted power ( $P_t$ ) and can be expressed as:

$$R = \frac{P_r}{P_i} = \left( \frac{\vec{E}_r}{\vec{E}_i} \right)^2 = |\tilde{r}|^2 \quad (1.13a)$$

$$T = \frac{P_t}{P_i} = \frac{\tilde{n}_t}{\tilde{n}_i} \left( \frac{\vec{E}_t}{\vec{E}_i} \right)^2 = \frac{\tilde{n}_t}{\tilde{n}_i} |\tilde{t}|^2 \quad (1.13b)$$

Since the spacers we use (air, hBN, SiO<sub>2</sub>) to create our optical cavities have purely real indices of refraction, these materials do not dissipate power, and the exclusive light absorption by graphene is given by:

$$A_{gr} = 1 - R_N - T_N \quad (1.14)$$

This model predicts an exclusive light absorption of about 2.3% for SLG (4.6% for BLG) in vacuum, which agrees with previous experiments [29].

### 1.4.2 Modeling Raman factor

When modelling the Raman factor, we must consider the interferences due to the multiple reflections of both incident and Raman scattered light [41–43]. The experimentally measured Raman scattered intensity,  $I$ , can then be found as,

$$I = F_{Gr} I_i \quad (1.15)$$

where  $F_{Gr}$  is the total enhancement factor (Raman factor) and  $I_i$  is the intrinsic Raman intensity of the material [41,44]. The Raman factor enhancement is calculated using the equation [44]:

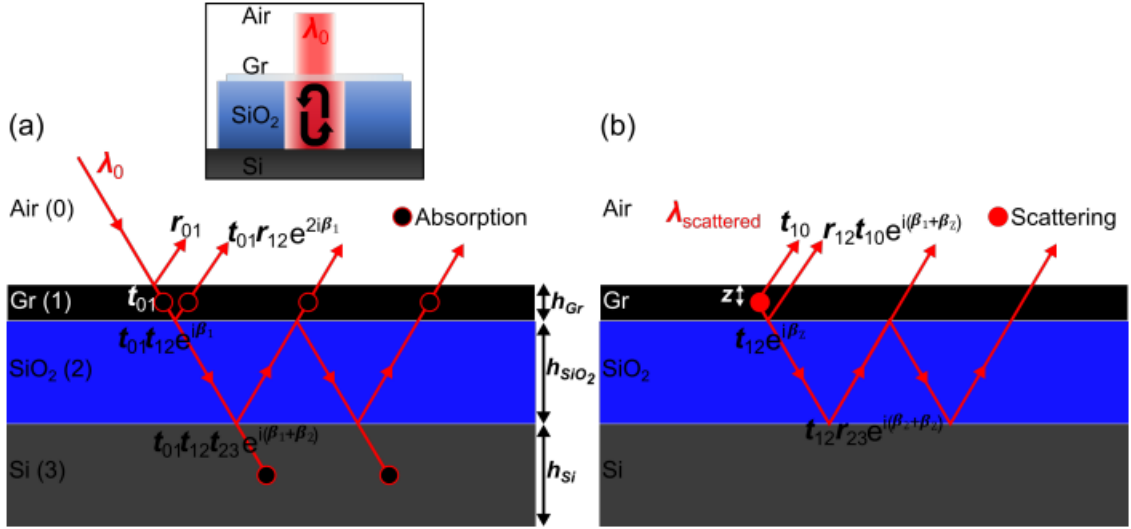


Figure 1.9: Schematic of reflection interferences both before (a) and after (b) Raman scattering for an air/Gr/SiO<sub>2</sub>/Si heterostructure. Fresnel equations are used to calculate the transmission and reflection amplitudes. Figure reproduced from [25]

$$F_{Gr} = N \int_0^{h_{Gr}} |F_{ab} F_{sc}|^2 dz \quad (1.16)$$

Here the first term,  $F_{ab} = \vec{E}_z / \vec{E}_0$ , is related to the net absorption, the second term,  $F_{sc} = \vec{E}_{out} / \vec{E}_{Ram}$ , to the scattering process,  $h_{Gr}$  is the thickness of graphene

(the material in which the interactions occur), and  $N$  is the normalization constant. For graphene,  $N$  is equal to the reciprocal of the Raman factor of free-standing graphene surrounded by vacuum. The two optical processes  $F_{ab}$  ( $\lambda = \lambda_{laser}$ ) and  $F_{sc}$  ( $\lambda = \lambda_{Raman-shifted}$ ) can be expressed for any number of media,  $N_{med}$ , using recursive equations:

$$F_{ab, N_{med}} = \tilde{t}_{01} \frac{e^{-i\tilde{\beta}_z} + \tilde{r}_{N-1_{med}} e^{-i(2\tilde{\beta}_1 - \tilde{\beta}_z)}}{1 + \tilde{r}_{N-1_{med}} \tilde{r}_{01} e^{-2i\tilde{\beta}_1}} \quad (1.17a)$$

$$F_{sc, N_{med}} = \tilde{t}_{10} \frac{e^{-i\tilde{\beta}_z} + \tilde{r}_{N-1_{med}} e^{-i(2\tilde{\beta}_1 - \tilde{\beta}_z)}}{1 + \tilde{r}_{N-1_{med}} \tilde{r}_{01} e^{-2i\tilde{\beta}_1}} \quad (1.17b)$$

where  $\beta_i$  are the phase shifts introduced in each medium ( $\beta_z$  in the graphene layer), and  $\tilde{t}$  and  $\tilde{r}$  are the previously introduced Fresnel coefficients for transmission and reflection. As an example, the devices proposed in the Chapter 3 will consist of four media: air, bilayer graphene, air, and aluminum; the equations for our optical processes can then be expressed as:

$$F_{ab,4} = \tilde{t}_{01} \frac{\left(1 + \tilde{r}_{12} \tilde{r}_{23} e^{-i\tilde{\beta}_2}\right) e^{-i\tilde{\beta}_z} + \left(\tilde{r}_{12} + \tilde{r}_{23} e^{-i\tilde{\beta}_2}\right) e^{-i(2\tilde{\beta}_1 - \tilde{\beta}_z)}}{1 + \tilde{r}_{12} \tilde{r}_{23} e^{-i\tilde{\beta}_2} + \left(\tilde{r}_{12} + \tilde{r}_{23} e^{-i\tilde{\beta}_2}\right) \tilde{r}_{01} e^{-2i\tilde{\beta}_1}} \quad (1.18a)$$

$$F_{sc,4} = \tilde{t}_{10} \frac{\left(1 + \tilde{r}_{12} \tilde{r}_{23} e^{-i\tilde{\beta}_2}\right) e^{-i\tilde{\beta}_z} + \left(\tilde{r}_{12} + \tilde{r}_{23} e^{-i\tilde{\beta}_2}\right) e^{-i(2\tilde{\beta}_1 - \tilde{\beta}_z)}}{1 + \tilde{r}_{12} \tilde{r}_{23} e^{-i\tilde{\beta}_2} + \left(\tilde{r}_{12} + \tilde{r}_{23} e^{-i\tilde{\beta}_2}\right) \tilde{r}_{01} e^{-2i\tilde{\beta}_1}} \quad (1.18b)$$

The incident wavelength (532 nm) is used in the absorption term, while the wavelengths related to the G or 2D peaks of graphene's Raman spectrum are used in the scattering term. The wavelengths related to these peaks are calculated using,

$$\omega_{Ram} (cm^{-1}) = \left| \frac{1}{\lambda_0 (nm)} - \frac{1}{\lambda_{sc} (nm)} \right| * 10^7 \quad (1.19)$$

where we find that the scattering wavelength related to the G peak is 581 nm ( $1580 cm^{-1}$ ) and that for the 2D peak is 621 nm ( $2700 cm^{-1}$ ).

Figure 1.10(a) shows the Raman factor enhancement at each of these wavelengths for an air/BLG/SiO<sub>2</sub>/Si device as a function of the oxide spacer thickness, as well as the exclusive light absorption of the BLG ( $A_{BLG}$ ). We see that absorption maxima correspond with unshifted Raman factor ( $F_{BLG-noshift}$ ) maxima, as these

are both calculated at the incident wavelength ( $\lambda_{laser} = 532$  nm), while the G and 2D peak maxima ( $F_{BLG-G}$  and  $F_{BLG-2D}$ , respectively) are shifted due to the change in wavelength ( $\lambda_G = 581$  nm and  $\lambda_{2D} = 621$  nm). The expected Raman factor decreases as the cavity height ( $h_{SiO_2}$ ) approaches the Raman shifted wavelengths.

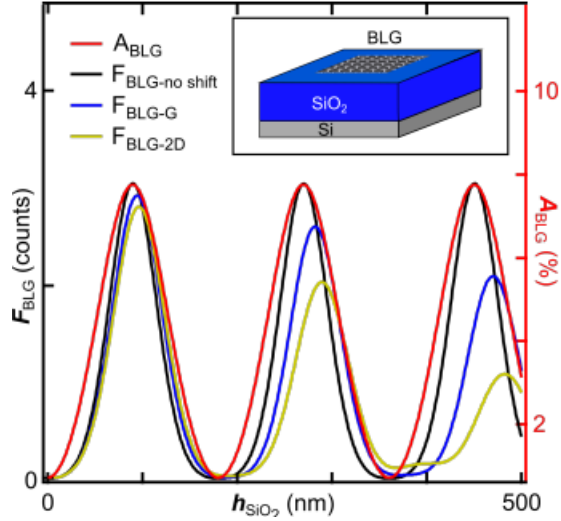


Figure 1.10: Exclusive light absorption and Raman factor of BLG heterostructures. Raman factors (left axis) and exclusive light absorption (right axis) of BLG in an air/BLG/SiO<sub>2</sub>/Si heterostructure (inset). Figure reproduced from [25].

## 1.5 Thesis organization

Most of the original work contained in this thesis is presented in Chapters 2 and 3, with some of the theoretical work presented in Section 1.4. In Chapter 2, we describe the fabrication of BLG optical cavities using our novel deterministic transfer process, where each step is described in turn. Our process utilizes a highly transparent, soluble nitrocellulose micro-stamp, which combines flexibility and adhesion in order to dry pick-up and transfer 2D crystals. After highlighting some transfer capabilities, we demonstrate that no significant defects, nor doping, are introduced during the transfer process by means of Raman spectroscopy. Our fabrication success rate was 95% for on-substrate devices and 93% for suspended devices. We then walk the reader through our data analysis process which converts our measured quantity, counts, into our desired quantity, Raman factor. We finally demonstrate a quantitative agreement between Raman scattering intensity from a partially suspended BLG (over SiO<sub>2</sub>)

optical cavity and the Raman factor predicted by our model. This agreement supports that we can transfer both on-substrate and suspended crystals of sufficient quality to manipulate their Raman factor and exclusive light absorption. With this cavity, we were able to enhance Raman scattering two-fold (vs BLG in vacuum), as well as tune the G peak Raman factor by 3.8 and the exclusive light absorption by 6.3 in a single device.

In Chapter 3, in order to enhance Raman scattering and light absorption, we introduce a highly reflective Al mirror to our heterostructures, which also serves as a mean to electrostatically tune our optical cavity height. We first fabricated on-substrate optical cavities where graphene was transferred over hBN and Al. These cavities demonstrated that Raman scattering can be tuned by a factor of 19 with cavity height differences on the order of 75 nm. We then present our platform for tuning optical cavity height *in-situ* and our first suspended BLG optical cavity over Al. We provide an overview of the measurement and the data analysis processes before presenting our Raman data when applying 0 V. Here we further validate our Raman scattering model and demonstrate our ability to detect changes in cavity height on the order of 1 nm using Raman factor, as well as tune Raman factor by 1.8 over a 10 nm change in height in the same device. We finally tune the applied voltage to our suspended BLG optical cavity, demonstrating an ability to electrostatically tune Raman factor by  $\approx 20\%$  and cavity height by  $\approx 3$  nm with the application of 500 mV.

In Chapter 4 we summarize the major results of this thesis: the novel deterministic transfer process which we use to fabricate pristine optical cavities, the agreement between our Raman scattering model and our measured data, which demonstrates our ability to enhance and tune both Raman factor and light absorption, and our ability to tune optical cavity height *in-situ* using electrostatic forces. We also present applications of NOEMS and a discussion on the future of this project. We show the ongoing fabrication of a BLG optical transducer, where small voltages can enhance/suppress light absorption for optical sensing.

## Chapter 2

# Fabrication of Bilayer Graphene Optical Cavities by Nitrocellulose Micro-stamp Transfer

In Chapter 1, we presented NOEMS [1–3] and optical cavities with an emphasis on light-matter interactions, notably the light absorption and Raman scattering which occur in graphene [28, 33, 34]. We also presented our models for graphene’s exclusive light absorption and Raman factor, which predicted that these characteristics can be enhanced by incorporating graphene in precisely assembled heterostructures. In order to study these light-matter interactions in detail, we must fabricate pristine optical cavities with as little disorder as possible. Moreover, we must fabricate suspended devices in order to access the mechanical properties of graphene, allowing for *in-situ* tunable control over the cavity thickness.

The deterministic and dry transfer of any-stacking-order [14, 45, 46] and suspended 2D materials such as SLG and BLG had been, so far, out of reach. Firstly, the dry pick-up of naked (not encapsulated) 2DMs on SiO<sub>2</sub> substrates, which permits for optical characterization of exfoliated 2DMs [47], has not been possible due strong adhesion to SiO<sub>2</sub> [5]. Secondly, it is challenging to deterministically [13] pick-up and transfer a single 2DM crystal while leaving nearby flakes untouched and is best done with a three-dimensional micro-stamp [48]. Lastly, the stamping process of thin-suspended 2DMs requires great finesse to avoid tearing of the crystal, or collapse of the suspended 2DM due to capillary forces [49]. Moreover, planar 2D heterostructures

can act as optical interferometric cavities to greatly enhance light absorption and Raman scattering in 2DMs, including graphene [10,19,21,44] and 2D transition metal dichalcogenides [20].

In this chapter we describe the method which we developed [25,26] to pick up and deterministically transfer 2DMs to fabricate our optical cavities. Our transfer method is capable of stacking and suspending ultra-thin 2DMs, such as graphene, hBN and MoS<sub>2</sub>, using a single-step preparation nitrocellulose micro-stamp. We begin with a summary of how we produce our 2DMs by mechanical exfoliation. Next, we give a step-by-step walkthrough of our nitrocellulose-based stamping procedure and showcase some of the optical cavities which we produced. Our method produced a very high yield (95% for on-substrate and 93% for suspended devices) while introducing no significant defects to the 2D crystals, according optical and Raman data. We then walk the reader through the required steps to analyze our Raman data, acquired from these cavities, to extract the desired Raman factor. Finally, we showcase a quantitative agreement between the Raman data and our Raman factor model, which also demonstrates that Raman factor and light absorption can be tuned by 4 and 6 folds, respectively.

It must be noted that the author did not contribute in the development of the fabrication method, itself, but aided extensively in demonstrating its effectiveness (yield), and is a co-author of the published results in 2D Materials. The author also wrote a macro to extract Raman factor from Raman data, which reproduced the results of [25,26].

## 2.1 Mechanical exfoliation of 2D materials

In order to produce pristine optical cavities (Fig.1.5) we must first produce pristine 2DMs for their assembly; this is achieved by mechanical exfoliation. Our basic building blocks, graphene and hBN crystals, are exfoliated via the "Scotch Tape" method [50], as seen in Fig. 2.1a. We begin with highly-oriented pyrolytic graphite (HOPG) flakes (Kish Graphite B from Covalent Materials Corporation) and high quality hBN crystals (PT110 Powder CTR from Momentive Performance Materials). For the graphite, we do a coarse mechanical cleavage with a razor blade to generate the thinnest possible flakes. Then, we place these flakes (powder in the case of hBN)

on a 10 cm long piece of tape (Scotch for graphite, Nitto for hBN) and further cleave the 2DM by repeatedly folding the tape  $\approx 15$  times; a finished example of cleaved graphite can be seen in Fig. 2.1(a).

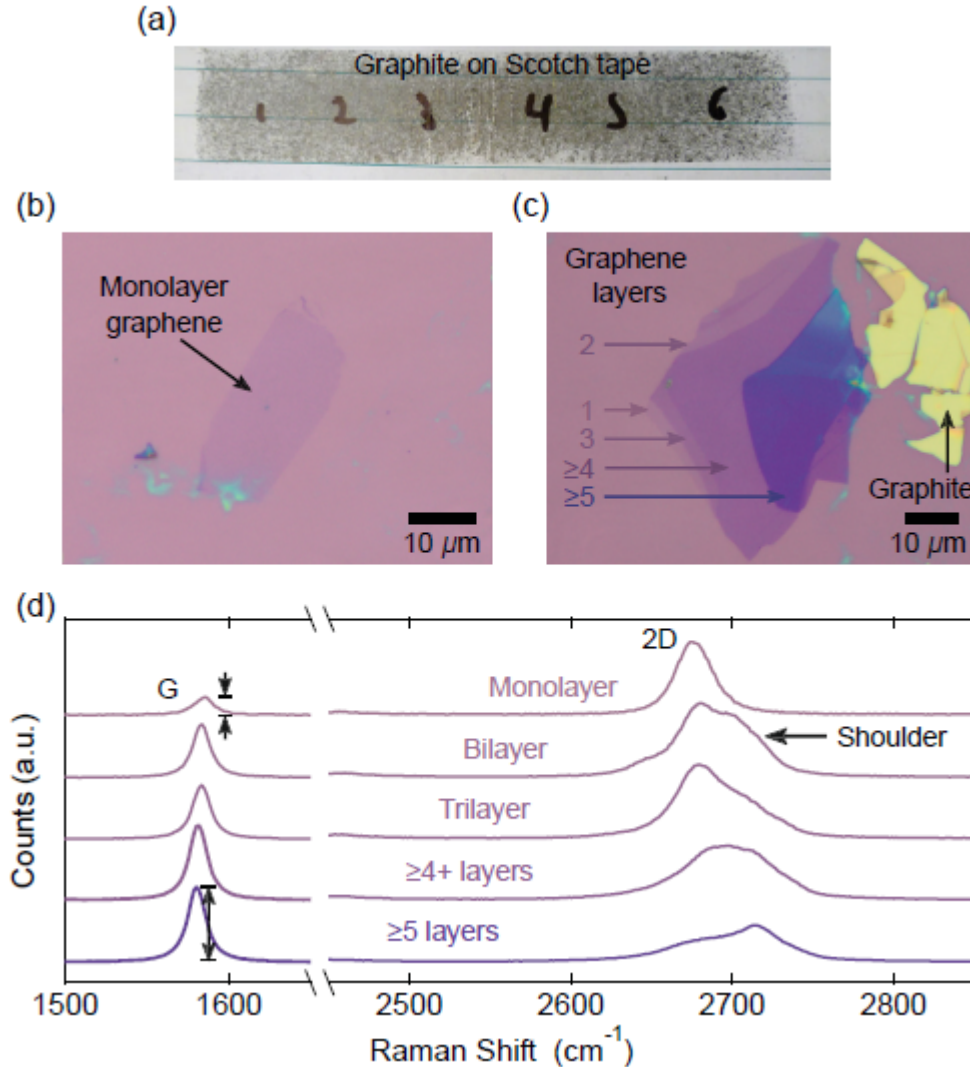


Figure 2.1: Exfoliation and characterization of BLG. (a) Graphene-covered Scotch tape after cleavage. (b) Optical image of a monolayer graphene crystal. (c) Optical image showing the colour contrast of graphene crystals with varying number of layers. (d) Normalized and offset Raman spectra of the locations indicated in (c), demonstrating the evolution of graphene's G and 2D peaks as the number of layers increases. The G peak becomes relatively larger in comparison to the 2D peak as the number of layers increases; the 2D peak broadens and acquires a 'shoulder' as the layers increase. Figure reproduced from [51].

The substrates onto which the graphene and hBN are then exfoliated are made of

500 $\mu\text{m}$ -thick silicon (Si) wafers with a 90 nm or 310 nm-thick film of silicon dioxide ( $\text{SiO}_2$ ). They are diced to  $\approx 5 \times 5$  mm to fit into our chip carriers for electronic measurements. A photolithography-patterned coordinate system is first transferred to these substrates to easily locate candidate 2DM crystals. Also, before transferring the exfoliated 2DM from the tape, the substrate is lightly etched with a dilute hydrochloric acid (HCl) and hydrogen peroxide ( $\text{H}_2\text{O}_2$ ) solution (18:1:1) at  $75^\circ\text{C}$  for 5 minutes to get rid of any surface residues. This process minimizes contamination of the 2DM from the substrate and promotes adhesion between the 2DM crystals and the oxide. The substrate is rinsed with DI water and blown dry with nitrogen before being baked at  $120^\circ\text{C}$  for 2 minutes to evaporate any leftover water. Finally, the tape containing the 2DM flakes is pressed on the substrate firmly using one's finger, and we wait approximately 10 minutes before slowly peeling off the tape (0.1 mm/s) with the help of tweezers.

Graphene and hBN crystals are first located using an optical microscope, and a rough estimate of their thickness (number of layers) can be made based on their colour contrast, as seen in Fig. 2.1(b)(c). The number of layers of candidate graphene crystals are then confirmed via Raman spectroscopy. The G peak of BLG is nearly as tall as its 2D peak, which now presents as a combination of four Lorentzians, as opposed to the single Lorentzian of its single-layer counterpart, as seen in Fig. 2.1(d). For our purposes, these crystals must be of uniform thickness in the region used in our optical cavities, and, for suspended devices, must also be as large as possible ( $> 25\mu\text{ m}^2$ ), so that the supported area exceeds the suspended area. This reduces the likelihood of slippage and collapse during measurements.

As for our hBN crystals, the naturally-occurring u-shaped cavities which we see after exfoliation present ideal platforms on which we can suspend our graphene. Here we look for cavities which are as wide as possible ( $\geq 1.5\mu\text{m}$ ) for maximum suspension lengths of  $\approx 5\mu\text{m}$ . This width is necessary since our laser spot diameter is on the order of  $\approx 1\mu\text{m}$ . As of yet, the maximum suspension length which we have achieved using this transfer method is  $6.2\mu\text{m}$ . The thickness of hBN flakes can also be estimated based on their colour, and atomic force microscopy (AFM) is finally used to quantify the exact heights along the cavity, as seen in Fig. 2.2. With the exfoliation and characterization of our basic building blocks complete, we can now move to the assembly of our optical cavities.

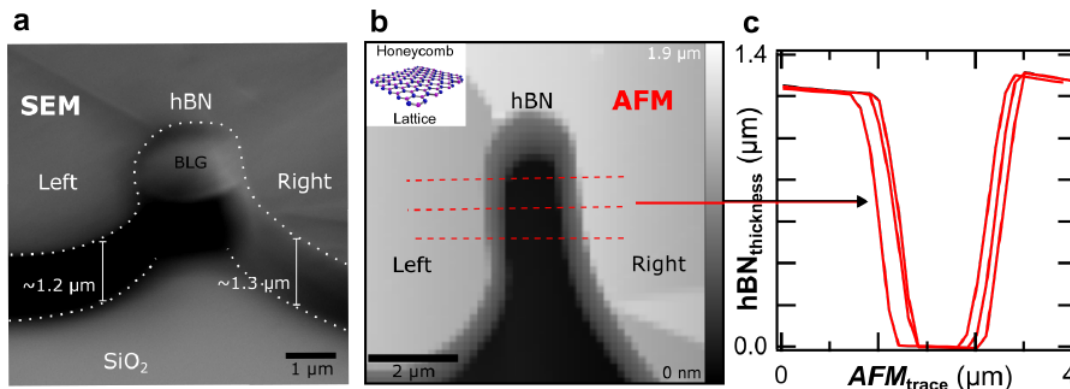


Figure 2.2: Characterization of hBN cavity. (a) Tilted SEM image (60 degrees) with approximated cavity height (solid lines). (b) AFM scan image with line traces plotted in (c). Figure reproduced from [26].

## 2.2 Nitrocellulose-based micro-stamp transfer method

To our knowledge, there were no methods [14,45,46] which could deterministically dry-transfer, in any stacking order, and suspend ultra-thin 2DM, such as SLG and BLG. Firstly, the dry pickup of naked (not encapsulated) 2DM from SiO<sub>2</sub> substrates had not been achieved due to strong adhesion between the 2DM and their substrates [5]. Secondly, it is a challenge to pick up a single crystal while leaving any nearby crystals untouched and ideally performed using a 3D micro-stamp [48]. Lastly, suspending 2DM requires finesse in order to avoid tearing the crystal or the crystal collapsing due to capillary forces [49].

To fabricate optical cavities we use our recently-published method [25]. This method is summarized in Fig. 2.3 and uses a nitrocellulose micro-stamp, which combines softness and adhesion, to dry pickup and transfer naked 2DM crystals. This method can be used to fabricate both suspended and on-substrate optical cavities.

We first prepare a nitrocellulose micro-stamp and locate the 2DM we wish to transfer on its original SiO<sub>2</sub> substrate (Fig. 2.3(a)). The micro-stamp is then aligned above the 2DM before being brought down into contact (Fig. 2.3(b)). After allowing for adhesion between the micro-stamp and 2DM, the 2DM is picked up by retracting the stamp (Fig. 2.3(c)). The new target substrate is then placed under the micro-stamp and the 2DM aligned before being lowered into contact (Fig. 2.3(d)). The

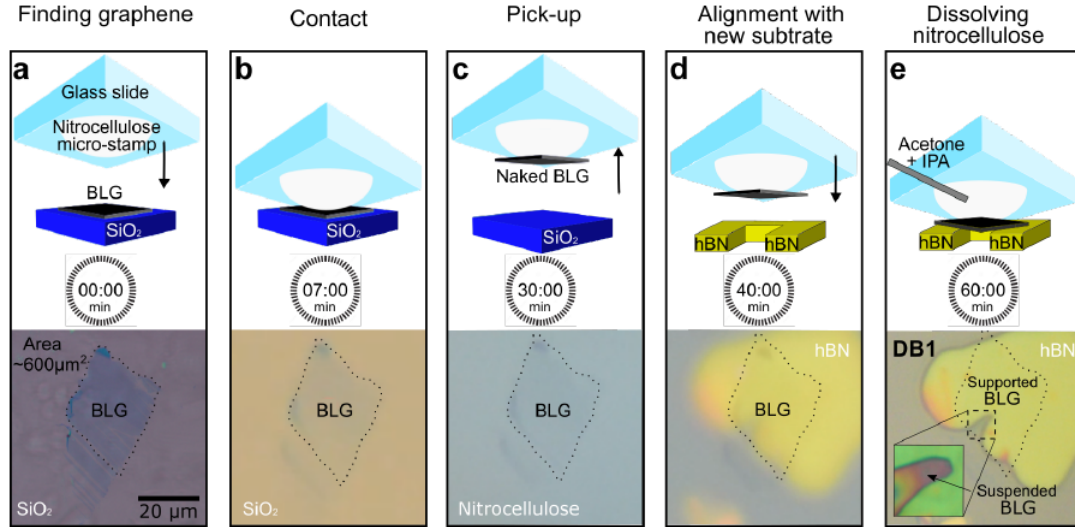


Figure 2.3: Step-by-step assembly of suspended graphene heterostructure. (a) Finding the BLG crystal through the transparent nitrocellulose micro-stamp. (b) Lowering the micro-stamp into contact with the BLG crystal and its immediate surroundings produces a pink/orange colour. (c) Direct pickup of the BLG crystal from the substrate. The crystal can be seen on the micro-stamp after refocusing. (d) Alignment of the BLG crystal over the target hBN cavity. (e) Dissolving the nitrocellulose micro-stamp using acetone and IPA. Figure reproduced from [25].

micro-stamp is then dissolved to complete the transfer using  $\mu\text{L}$  amounts of solvents (Fig. 2.3e) [52]. Before outlining the details of these steps we first present our stamping apparatus.

### 2.2.1 Stamping apparatus

The stamping apparatus used to raise/lower our micro-stamps and align them with our 2DM and substrates is shown in Fig. 2.4. The main features are a rotating stage with an integrated vacuum to hold and orient substrates, a 3D micro-manipulator which holds the glass slide on which we deposit our micro-stamp, and a long working distance optical assembly leading to a high resolution CCD camera for live viewing. This apparatus was inspired by other deterministic transfer techniques [4, 53–55].

### 2.2.2 Nitrocellulose micro-stamp preparation

Before preparing the micro-stamp we must first clean the crystal for pick-up. With a BLG crystal chosen and characterized, we submerge its substrate in a warm bath

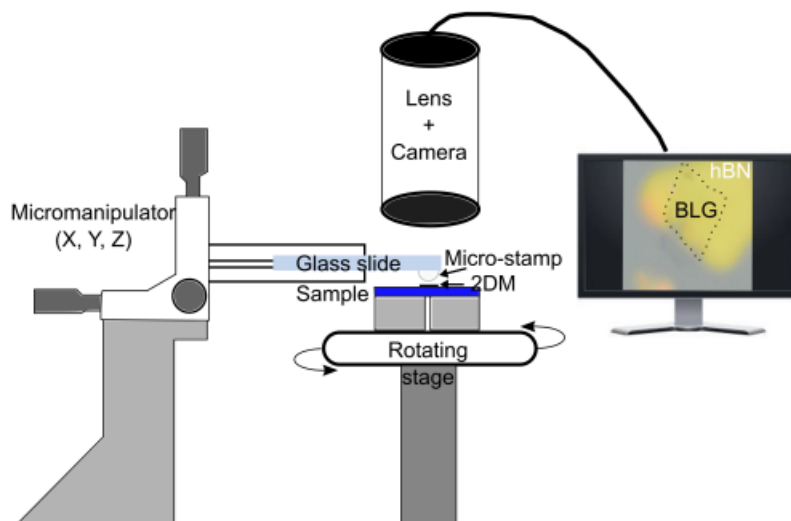


Figure 2.4: Stamping apparatus. The substrates from which we pick up and to which we transfer our 2DM are held by vacuum on the rotating stage. The micromanipulator holds the glass slide containing the micro-stamp and controls its position. A long working distance optical assembly is in place for live viewing of the transfer. Figure reproduced from [25].

of acetone at  $75^{\circ}\text{C}$  for 5 minutes, rinse with isopropyl alcohol (IPA), then rinse with DI water and bake it at  $120^{\circ}\text{C}$  for 2 minutes. The substrate is then mounted on the vacuum stage of our stamping apparatus and the camera focused on the desired crystal. The vacuum stage is rotated such that the crystal has the desired orientation.

We then prepare the micro-stamp on a glass slide: we submerge the tip of a 1 mL syringe in our nitrocellulose solution (nail polish, Revlon - Extra Life<sup>TM</sup> No Chip Top Coat) (Fig. 2.5(a)) and then deposit a small droplet on a glass slide to form our micro-stamp (Fig. 2.5(b)). Ideally the stamp will possess a contact area (top of stamp, appears brighter under optical microscope) that is  $\approx 200\mu\text{m}$  in diameter, as seen in Fig. 2.5(c). Smaller contact areas ( $\approx 50\mu\text{m}$  diameter) have been achieved, though this is also the area which acts as a lens to align the 2DM during the transfer process, where greater visibility is advantageous.

### 2.2.3 Making contact and pick up of naked 2D crystal

The glass slide with the micro-stamp is then mounted on the micro-manipulator, as seen in Fig. 2.4, and then lowered until it is  $\approx 1\text{mm}$  above the 2DM to be transferred. The contact area of the stamp is then centered on the 2DM; the stamp, itself, is

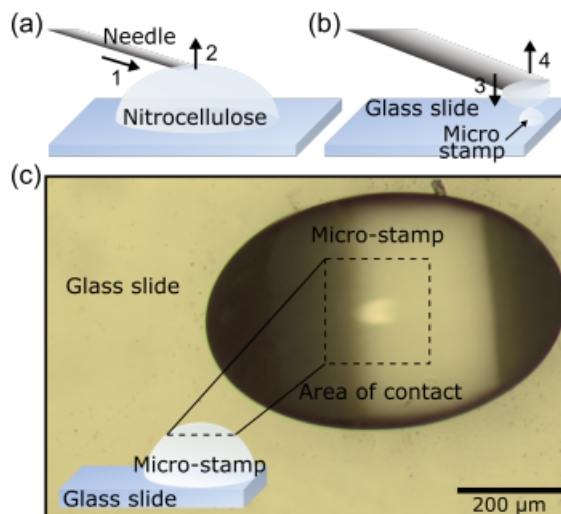


Figure 2.5: Nitrocellulose micro-stamp preparation. (a) A syringe tip is submerged in a droplet of nitrocellulose solution and then retracted such that a droplet remains due to capillary forces. (b) The syringe tip is lowered slowly such that the droplet barely touches the surface of the glass slide, leaving a micro-stamp. Top-view optical image of a micro-stamp, showing the bright white contact area which will be integral to the transfer process. Figure reproduced from [25].

transparent and acts as a lens due to its ellipsoidal shape. After waiting 6min for the stamp surface to sufficiently dry (harden), the stamp is lowered slowly to contact the selected crystal and its immediate surroundings. Contact is apparent when the stamp appears to change in colour to orange/pink (Fig. 2.3(b)).

After waiting  $18 \pm 2$  min (longer if the 2DM was not freshly exfoliated) to promote adhesion between the stamp and 2DM, the stamp is deftly raised and the 2DM picked up, as shown in Fig. 2.6. After raising the glass slide further, pick up can be confirmed by focusing on the micro-stamp (where one should see their 2DM) or on the empty substrate underneath.

#### 2.2.4 Alignment of 2DM with target substrate

Once the target substrate, such as an hBN cavity, is mounted, the camera is focused and the stage rotated such that the cavity has the desired orientation. We trace the hBN cavity contour on our video screen for reference when aligning the 2D crystal. The micro-stamp is then centred above the hBN cavity and progressively lowered (which includes refocusing and aligning) until the crystal and hBN cavity are both

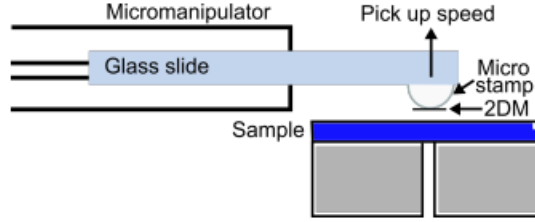


Figure 2.6: Schematic of the 2DM pick up process. The glass slide, held by the micro-manipulator is raised and the adhesion of the 2DM with the micro-stamp overcomes the VdW forces holding the 2DM to the substrate. Figure reproduced from [25].

clearly visible in focus, as seen in Fig. 2.7(a). The contour trace is erased and a final alignment correction is done before lowering the crystal into contact with the target, as seen in Fig. 2.7(b). We ensure that the micro-stamp is not pressed hard enough to deform the contact area, and does not contact the  $\text{SiO}_2$  immediately surrounding the hBN substrate, as shown in Fig. 2.7(c).

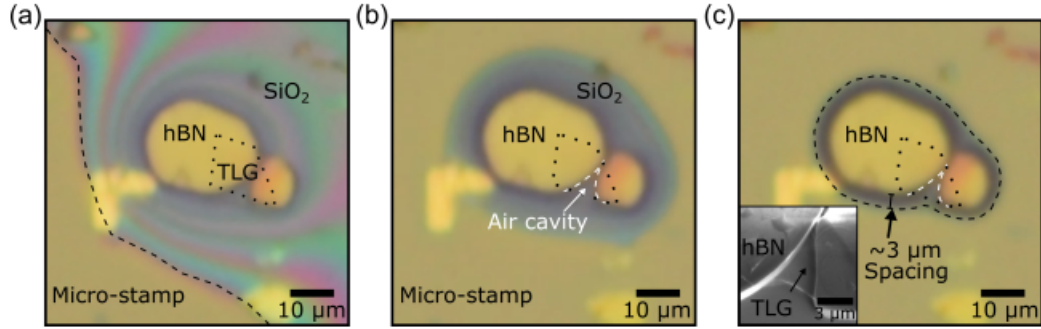


Figure 2.7: Alignment and stamping of trilayer graphene (TLG) on an hBN trench. (a) The TLG crystal is barely visible above the target hBN trench. The micro-stamp begins to make contact with the substrate. (b) The TLG crystal makes slight contact with the hBN trench. (c) The micro-stamp is in contact with the  $\text{SiO}_2$  substrate and hBN, but does not contact a 3  $\mu\text{m}$ -wide zone surrounding the hBN trench. Figure reproduced from [25].

## 2.2.5 Release of naked 2D crystal by dissolution of micro-stamp

To release the 2DM and complete the transfer, a micro-pipette is used to inject one drop of acetone ( $500\mu\text{L}$ ) in the spacing between the micro-stamp and substrate, dissolving the stamp and releasing the 2DM, as shown in Fig. 2.8(a). Additional

droplets are added to ensure that the nitrocellulose is completely dissolved and reduce the risk of excess residues. The glass slide is then raised ( $\approx 0.5$  mm) and we do a local rinsing with IPA using the same micro-pipette, as shown in Fig. 2.8(b). This rinsing process is repeated multiple times to completely flush the acetone and polymer residues. The final, evaporation step of this procedure must be controlled, as capillary forces could potentially collapse the suspended 2DM. We control the evaporation rate by raising or lowering the glass slide while controlling its position, eliminating the need for critical point drying, as shown in Fig. 2.8(c)(d). This is crucial to ensure that the risk of collapse is minimized for suspended 2DM.

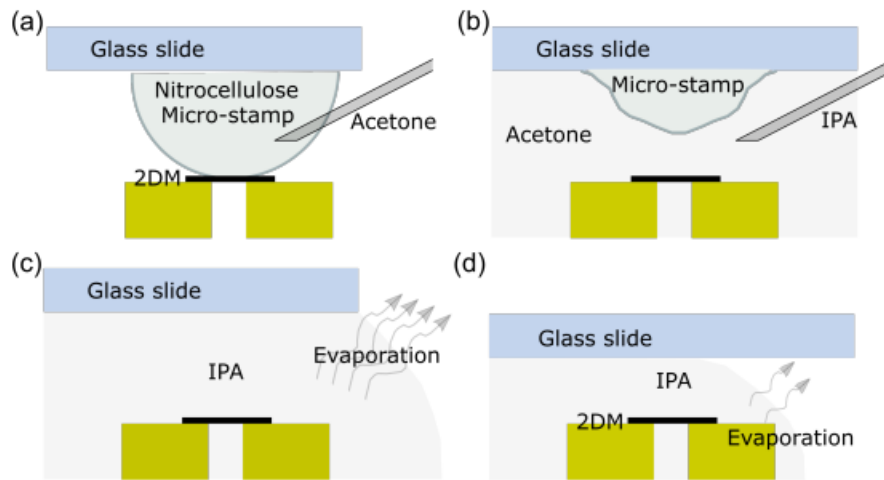


Figure 2.8: Dissolution of the nitrocellulose micro-stamp to complete the transfer procedure. (a) A micro-pipette is used to introduce a drop of acetone. (b) The acetone dissolves the micro-stamp and the 2DM is released. IPA is introduced to flush the acetone and polymer residues. (c) The stamp is completely dissolved and the IPA begins to rapidly evaporate. (d) The evaporation rate can be controlled by lowering the glass slide, minimizing the risk of collapse for suspended crystals. Figure reproduced from [25].

## 2.2.6 Supported and suspended 2D material heterostructures

With the deterministic transfer method presented in Fig. 2.3 we can fabricate both supported (on-substrate) and suspended heterostructures; Figure 2.9 showcases some of the structures produced by the author. The transfer method possesses a translational accuracy of  $1\mu\text{m}$  and a rotational accuracy of  $1^\circ$ , as demonstrated in

Fig. 2.9(a). Out of the 15 suspended heterostructure assemblies we attempted, 14 were successful.

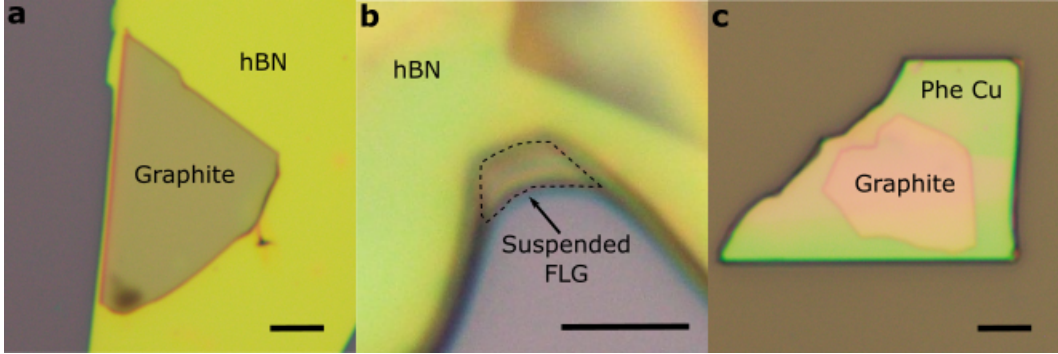


Figure 2.9: 2DM heterostructures. (a) Graphite which has been transferred to hBN, demonstrating our method’s translational ( $1\mu\text{m}$ ) and rotational ( $1^\circ$ ) accuracy. (b) Few-layer graphene (FLG) that has been suspended above  $\text{SiO}_2/\text{Si}$  by means of an hBN trench. (c) Graphite that has been transferred onto phenol-copper, a material which is used in chiral-induced spin selectivity (CISS) measurements [56]. All scale bars are  $4\mu\text{m}$ .

While graphite and graphene are the most common 2DM which we have transferred, this method is also capable of dry picking up naked hBN and  $\text{MoS}_2$ , as seen in Fig. 2.10, which showcases some of our high-quality and large area 2D heterostructures. Both the optical and the Raman data presented confirm a low defect density in the transferred crystals. To assemble the heterostructures visible in Fig. 2.10(b, e), we first evaporated a 50 nm-thick aluminium (highly reflective material) film onto our  $\text{SiO}_2/\text{Si}$  wafer, which will act as a backplane mirror for an optical cavity, as discussed further in Chapter 3. We next transferred thick ( $\approx 400$  nm) and large area (up to  $\approx 1000\mu\text{m}^2$ ) hBN crystals to act as substrates for the ultra-thin crystals and define the thickness of the optical cavity heterostructures. We then picked up and deterministically transferred the large area 2DM crystals, seen on their initial  $\text{SiO}_2$  substrates in Fig. 2.10(a, d, g). We note that the entire areas of these target crystals were transferred without tearing or folding, and with very few small bubbles visible in the transferred crystals, shown in Fig. 2.10(b, e, h). The Raman data seen in Fig. 2.10(c, f, i) were taken at the red marker locations shown in the corresponding optical images. The relative heights of the Raman peaks, such as the G and 2D peaks of graphene, are affected after the assembly of the optical cavity heterostructures, as expected. The ratio between the area of the G and 2D peaks also

changes, though this is dependant on the device geometry [33]. We also see that the width of the Raman resonances are the same before and after transfer, and that there is a negligible D peak in the graphene spectra, indicating that no major disorder was introduced in the stamping of these crystals [36,49,57,58]. Out of the 21 on-substrate heterostructure assemblies we attempted, 20 were successful.

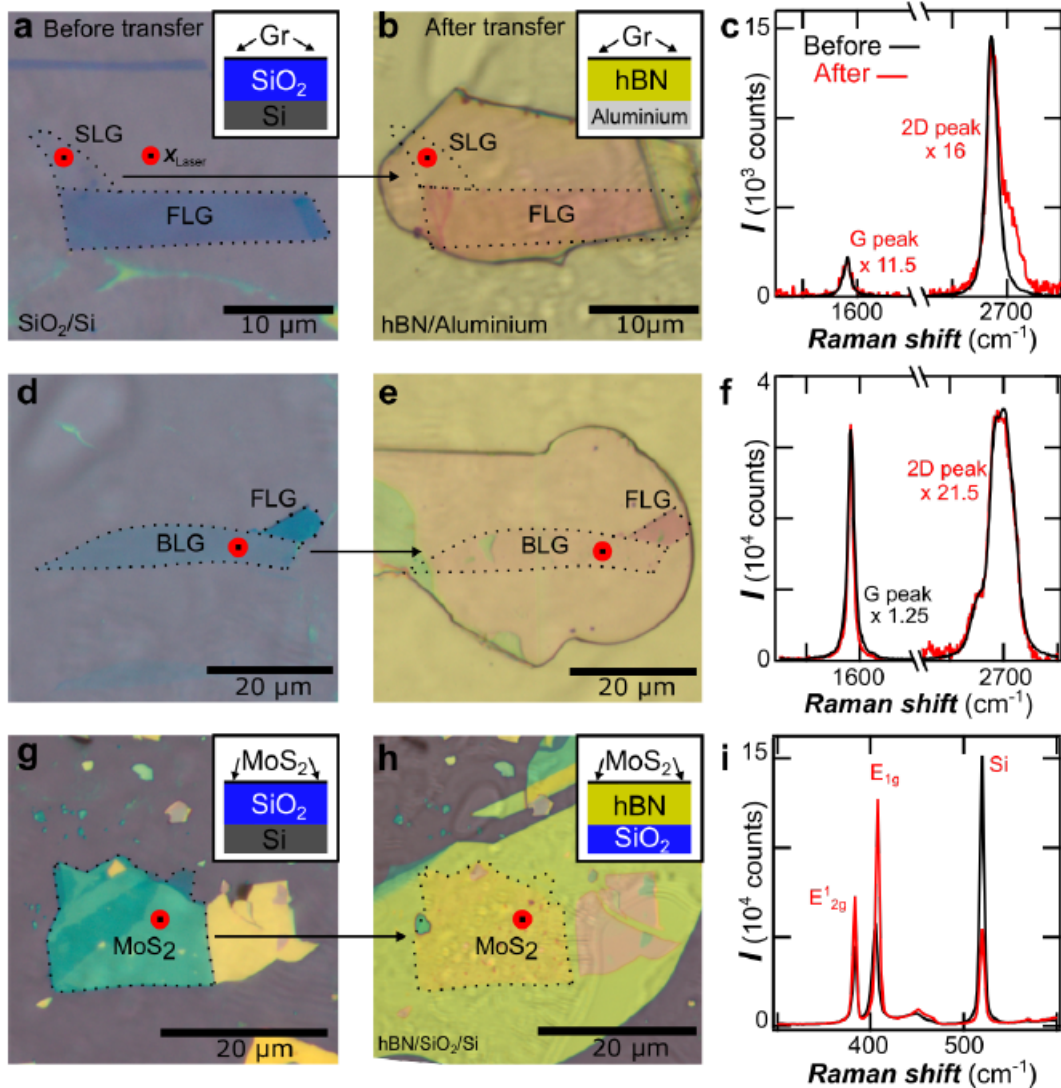


Figure 2.10: On-substrate heterostructures. (a) Optical image of SLG crystal before and (b) after transfer. The red dot is the location of the Raman scan. Insets: illustrations of device profiles. (c) Raman spectra before (black) and after (red) transfer. (d) Optical image of BLG crystal before and (e) after transfer. (f) Raman spectra before (black) and after (red). (g) Optical image of MoS<sub>2</sub> crystal before and (h) after transfer. (i) Raman spectra before (black) and after (red). Figure reproduced from [26].

## 2.3 Determining the Raman factor of graphene from experimental data

With graphene devices fabricated it is possible to experimentally verify that our model for Raman factor, presented in Chapter 1.5.2, is correct. To do so, a standard was established in order to systematically and confidently convert our experimental data (counts) to Raman factor. This standard, described in the subsections to follow, is broken down into 3 steps:

1. Theoretically calculate a Raman factor for the graphene on its initial substrate.
2. Measure and normalize the Raman events which occur in the graphene on the initial substrate to relate measured data and theory (calibration).
3. Measure the Raman events which occur in the graphene once it has been transferred to its new substrate to extract a Raman factor experimentally.

### 2.3.1 Modelling the Raman factors of graphene on silicon dioxide

Our graphene is exfoliated onto SiO<sub>2</sub>/Si chips for optical and Raman characterization of its number of layers, so we first calculate a Raman factor for the graphene on this substrate. The thickness of our SiO<sub>2</sub> layer is measured via ellipsometry to be  $(90 \pm 5)$ nm. Modelling the Raman factor for an air/BLG/SiO<sub>2</sub>/Si geometry, as seen in Fig. 2.11, we determine that the Raman factors associated with graphene on this initial substrate are  $F_{BLG-G} = 2.8 \pm 0.1$  for the G peak and  $F_{BLG-2D} = 2.7 \pm 0.1$  for the 2D peak.

### 2.3.2 Extracting an experimental Raman factor

Next, we associate intensities (counts) which have been normalized to account for the laser power taken at the time of each measurement to these Raman factors. Once Raman data for our bilayer flake has been acquired, we begin our analysis by fitting the G and 2D peaks of the Raman spectrum, as seen in Fig. 2.12(a,b), in order to extract the integrated counts under each peak. The G peak is fit with a single Lorentzian of the form:

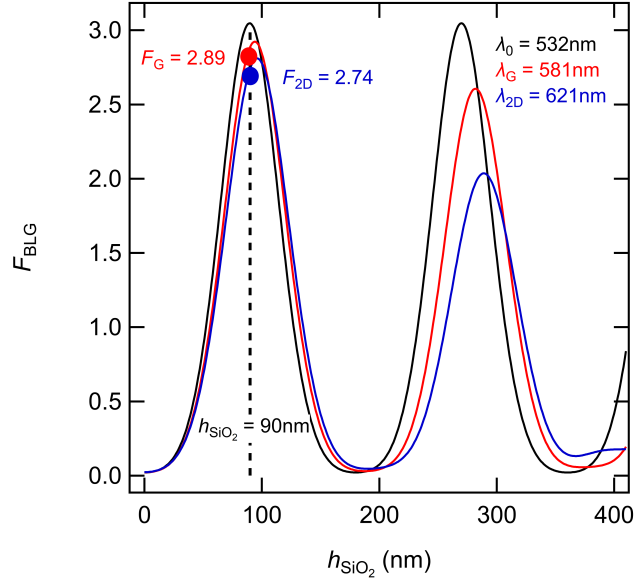


Figure 2.11: Raman factor of bilayer graphene on a SiO<sub>2</sub>/Si substrate. Our graphene is exfoliated onto  $\approx 90$  nm of SiO<sub>2</sub> which gives  $F_G = 2.89$  and  $F_{2D} = 2.74$  for the wavelengths associated with the G and 2D peaks, respectively.

$$f(x) = y_0 + m * x + \left( \frac{2A}{\pi} \right) \left( \frac{FWHM}{4(x - x_0)^2 + FWHM^2} \right) \quad (2.1)$$

where  $y_0$  is the background offset,  $m$  is the slope of the background,  $x_0$  is the G peak position,  $A$  is the area under the peak, and  $FWHM$  is the full width at half maximum. Here the number of counts under the peak are extracted directly from the fit (area).

The 2D peak is similarly fit using a combination of four Gaussians:

$$f(x) = y_0 + m * x + \sum_{i=1}^4 A_i \exp \left( -4 \ln(2) * \left( \frac{x - x_i}{FWHM_i} \right)^2 \right) \quad (2.2)$$

where  $A_i$ ,  $x_i$  and  $FWHM_i$  are the amplitude, position and full width at half maximum of Gaussian  $i$ , respectively. The number of counts under the peak is then found using the equation:

$$Area = \frac{\sqrt{\pi}}{2\sqrt{\ln(2)}} \sum_{i=1}^4 A_i * FWHM_i \quad (2.3)$$

Since our Raman data can be taken at varying laser powers and with potentially

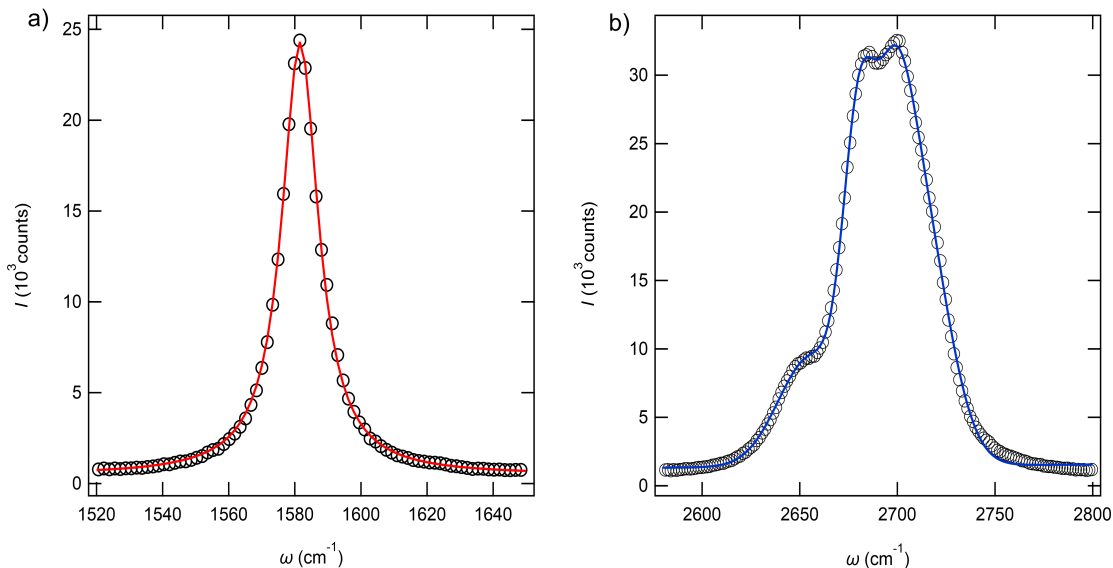


Figure 2.12: Example of fits (solid lines) for bilayer graphene G peak (a) and 2D peak (b) data (open circles).

different acquisition times, we must first normalize our integrated counts so that the associated Raman factor can be used to quantify subsequent measurements:

$$I/P_L \equiv \text{counts/power/time} \quad (2.4)$$

Figure 2.13(a) demonstrates that this determination of normalized counts is reproducible for arbitrary positions on different bilayer graphene flakes; Figure 2.13(b) demonstrates the same for different laser powers taken at the same position. The laser power was recorded before each 100 s dataset. Here we note that our laser power is generally in the 0.75 – 1 mW range when acquiring Raman factor data. Taking the average of the values presented in Fig. 2.13(a) gave normalized counts of  $I/P_{SiO_2} = 7.2 \text{ counts}/(\mu\text{ W} * \text{ s})$  and  $25.8 \text{ counts}/(\mu\text{ W} * \text{ s})$  for the G and 2D peaks, respectively.

## 2.4 Assigning Raman factors to experimental data and agreement with our model

The normalized counts measured experimentally ( $I/P_{SiO_2}$ ) correspond to the theoretically determined Raman factors ( $F_{SiO_2-G} = 2.8 \pm 0.1$  and  $F_{SiO_2-2D} =$

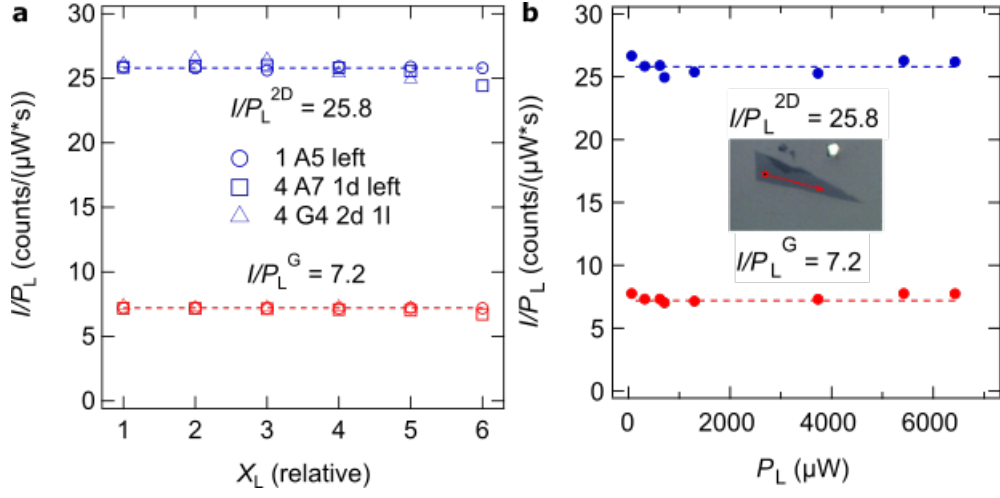


Figure 2.13: Normalized counts measured at arbitrary positions on BLG and taken with varying laser powers. (a) Normalized counts measured at arbitrary positions on three different bilayer graphene flakes (inset line map in (b) corresponds to open-circle data). (b) Normalized counts measured at one position (marked on inset) with different laser powers. The average of the normalized counts in (a) gives  $I/P_L^G = 7.2$  counts/ $(\mu\text{W} \cdot \text{s})$  and  $I/P_L^{2D} = 25.8$  counts/ $(\mu\text{W} \cdot \text{s})$ .

$2.7 \pm 0.1$ ), and this established our calibration. Once our graphene has been transferred to its new substrate and Raman data has been measured, we can use the relationship

$$\frac{F_{SiO_2}}{I/P_{SiO_2}} = \frac{F_{meas}}{I/P_{meas}} \quad (2.5)$$

in order to extract Raman factors from our experimental data for BLG inside of any heterostructure.

One of our optical cavities was fabricated with a height gradient (see Fig. 2.14(a)) in order to verify the accuracy of our experimental measurement of Raman factor. We observed quantitative agreement between our theoretical model and the G and 2D Raman factors which were extracted from Raman measurements, as shown in Fig. 2.14(b, c), as well as an ability to tune Raman factor by a factor of 4 in a single device. We note that our model also predicted that exclusive light absorption,  $A_{BLG} \approx 10\%$  for this geometry at a cavity height of  $h_{air} = 160\text{nm}$ , more than double the exclusive light absorption of BLG in vacuum, and can be tuned by a factor of 6 inside this heterostructure.

Having demonstrated agreement between our Raman factor model and our

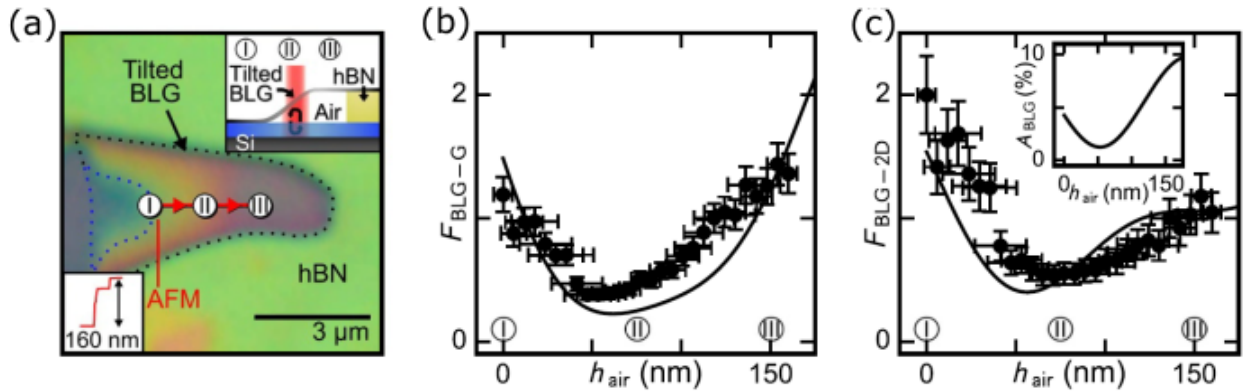


Figure 2.14: Experimental agreement with Raman factor model. (a) Top optical view of a transferred tilted-suspended BLG flake. Region I is supported by  $\text{SiO}_2$ , region II is suspended at heights ranging from 0 to 160nm, and region III is at a constant height of 160nm. The inset shows a cross-sectional view of the device's geometry. Raman factor as a function of cavity height for the G peak (b) and 2D peak (c). Experimental data is shown as solid markers and the solid trace is a zero-fit calculation using our model. The inset shows the exclusive light absorption of BLG for these same cavity heights.

experiments, we have shown that we can build suspended heterostructures of sufficient quality to tune the light-matter interactions in graphene via air spacer thickness,  $h_{\text{air}}$ , as seen in the inset of Fig. 2.14(a). Our next goal is to enhance light-matter interaction strength and add the ability to tune these interactions in-situ by means of an aluminium (Al) backplane mirror, as seen in Fig. 1.5. The Al mirror will also act as an electrode which will control  $h_{\text{air}}$ , thereby tuning Raman factor and exclusive light absorption, with a gate voltage.

## Chapter 3

# Enhancement of Graphene Light-matter Interactions in a BLG/air/Al Optical Cavity

In the previous chapters we presented the deterministic 2DM stamping procedure [25], Raman factor modelling, and measurements made to fabricate and characterize the enhancement of light-matter interactions in 2D heterostructures. We demonstrated that we can widely and quantitatively tune light absorption and Raman scattering in graphene [28, 33, 34]. Now, we aim to greatly increase the range over which we can suppress or enhance these interactions *in-situ* within a single device.

Developing 2DMs for optoelectronics applications [11] or exploring 2D light-matter interactions [2] requires increasing the very small bare light absorption in ultra-thin 2DMs [24]. While previous work focused on maximizing absorption of the infrared range [21, 59], we focus on the absorption of visible light by suspended BLG. Moreover, suspending BLG over an Al mirror would permit for tunable control of optical cavity thickness, and, consequentially, light absorption. We demonstrate quantitatively that light absorption enhancement is feasible and can be tuned *in-situ* in suspended BLG optical cavities, which could lead to high on-off ratio light-absorption transducers [60]. This will open up opportunities to generate strong light-matter interactions in 2D NEMS [19], and twisted BLG [10] NOEMS.

In this chapter, we present the addition of an aluminium mirror to our optical cavities, which serves to increase the enhancement of light-matter interactions, while

also providing a means to tune these interactions *in-situ* via an applied voltage. Measurements on on-substrate (hBN) BLG optical cavity devices with an Al back-plane mirror demonstrated that Raman scattering can be tuned by a factor of 19 with cavity thickness differences on the order of 75 nm. Also, Raman data from an optical cavity of BLG suspended over Al demonstrated that we can match our measured  $F_{BLG-G}$  to the theoretically calculated Raman factor produced by our model. Moreover, we demonstrated that Raman factor can be tuned 1.8x over a 10 nm change of  $h_{air}$  in the same device. According to our model, these measurements correspond to an exclusive light absorption of 15.6%, 3.4 times that of BLG in vacuum. Finally, once a gate voltage was applied, we were able to electrostatically tune Raman factor by 1.2 folds and  $h_{air}$  by  $\approx 3$  nm with the application of 500 mV. This proof of concept opens the door to further research at higher applied voltages, where we predict that Raman factor can be tuned by a factor of  $\approx 30000$  for  $\Delta V_g = 15$  V.

### 3.1 Enhancing Raman factor in BLG/hBN/Al optical cavities

We have shown in Section 1.4 that the exclusive light absorption and Raman scattering enhancement of BLG can be improved by factors of  $\approx 2$  and 3, respectively, when fabricating an optical cavity with an air/BLG/SiO<sub>2</sub>/Si geometry (see Fig. 1.10). We can improve these numbers further by replacing SiO<sub>2</sub>/Si with an Al mirror. Aluminium's high reflectance ( $> 90\%$  for visible light [61]) makes it an ideal substrate for an optical cavity in that: 1) more photons are reflected back to the BLG, increasing absorption, and 2) the effective optical cavity thickness will be more uniform due to a reduced penetration depth, lessening the effect of spurious destructive interference due to variations in cavity thickness. These effects are captured by our model when comparing optical cavities where BLG has been suspended over SiO<sub>2</sub>/Si (Fig. 3.1(a)) and Al (Fig. 3.1(b)) substrates. In Fig. 3.1(c), we see that not only is the Raman scattering enhanced 5-fold in the presence of an Al mirror, but the heights associated with constructive and destructive interference become more uniform for the wavelengths of light associated with the G and 2D peaks. We also predict a decrease in Raman scattering as the cavity thickness is increased and the effects of destructive interferences become more prevalent.

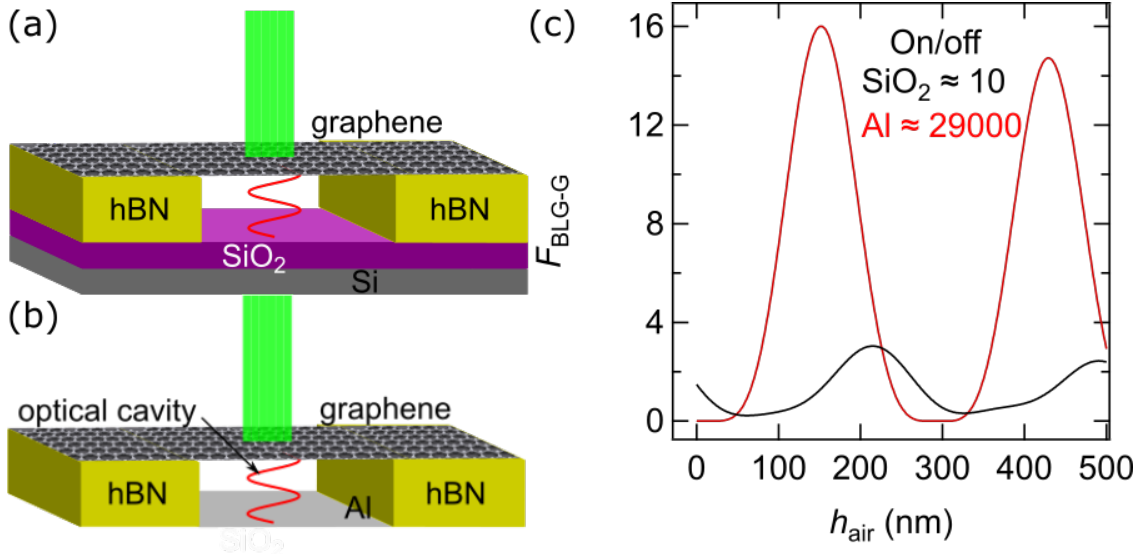


Figure 3.1: Comparing Si and Al as backplane mirrors in an optical cavity. (a) Schematic of a BLG optical cavity where it has been suspended over SiO<sub>2</sub>/Si. (b) Schematic of a BLG optical cavity where it has been suspended over Al. (c) G peak Raman factor,  $F_{BLG-G}$ , enhancement in the presence of an Al mirror. The Raman factor is greatly enhanced when suspending over Al (red) as opposed to SiO<sub>2</sub> (black). On/off ratios are also significantly increased from  $\approx 10$  over SiO<sub>2</sub> to  $\approx 29000$  over Al.

We have experimentally observed the tunability of BLG’s Raman scattering when supported over an Al mirror by hBN (BLG/hBN/Al), shown in Fig. 3.2. These cavities were fabricated by first depositing a layer of Al (procedure explained in the next section), followed by the transfer of hBN and BLG, in sequence. Figure 3.2(a) is a top view of one of four BLG/hBN/Al optical cavities which we fabricated with various spacer thicknesses. Figures 3.2(b, c) compare the measured G and 2D peak Raman factors (circles) from each of the cavities to those calculated by our model (solid curve). We see a strong quantitative agreement and also demonstrate that  $F_{BLG-G}$  can be tuned 19 folds. Moreover, our calculation of the exclusive light absorption (seen in the inset of Fig.3.2(c)) for this cavity geometry strongly supports that the exclusive light absorption of BLG, at the 532 nm laser wavelength, can be modulated from less than 1% to over 10%. However, these are supported heterostructures where the Raman factor (absorption) of the BLG is set by the thickness of the hBN substrates and will remain unchanged. Our goal is to build suspended BLG optical cavities, where the light-matter interactions can be tuned across a broad range within a single device.

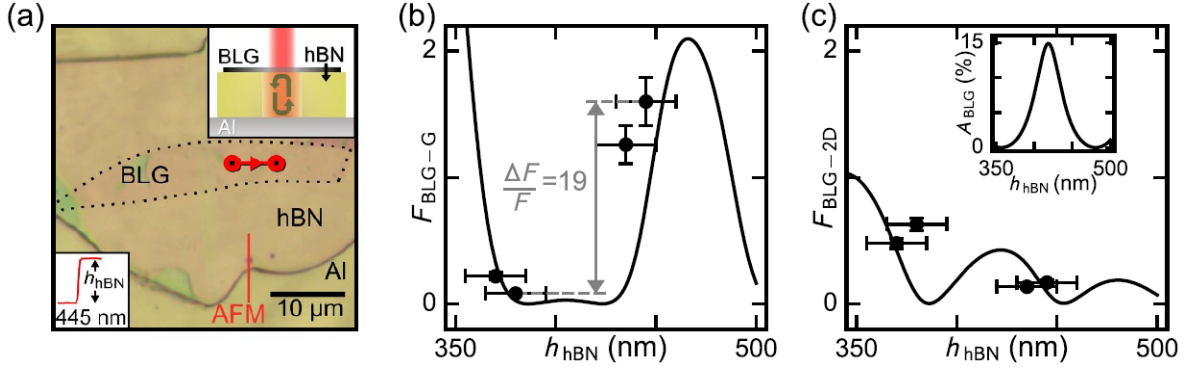


Figure 3.2: The tunability of BLG’s Raman factor when supported over Al. (a) Top view of an air/BLG/hBN/Al optical cavity (schematic of side view seen in top right inset). The lower left inset shows an AFM trace taken at the red line location. (b) G peak data and (c) 2D peak data from the cavity shown in (a), as well as similar cavities with varying  $h_{\text{hBN}}$ . The markers are experimental data and the solid traces were produced by our model. G peak Raman factor can be tuned 19 folds over a 75 nm difference in spacer thickness. The inset of (c) shows the predicted exclusive light absorption by BLG with this cavity geometry. Figure modified from [25].

## 3.2 Fabrication of BLG/air/Al optical cavities and instrumentation for Raman measurements

In order to simultaneously tune and measure the light-matter interactions of our graphene optical cavities, we need a platform that is capable of deflecting our graphene while Raman data is being collected. As mentioned previously, an Al mirror would not only enhance light-matter interactions, but can also act as an electrode with which we can apply an electrostatic force to the graphene, thereby tuning the optical cavity height. In the pages to follow, we describe how we fabricate our optical cavities suspended above Al for measurement and the Raman instrumentation with which the light-matter interactions are recorded.

### 3.2.1 Deposition of aluminium mirror and top electrode for in-situ electrostatic tuning

In order to apply an electrostatic force to our graphene we must deposit two aluminium electrodes onto our chips: one in the hBN trench which will act as the optical cavity mirror and one on top of the hBN which will lead to ground and

allow a voltage to be applied, as seen in Fig. 1.1(b). The initial mask-aligned photolithography process is summarized in Fig. 3.3(a). We begin by coating our chips in photoresist and spinning them to produce an even layer. The chip is then covered with a photomask which defines the electrode patterns and is exposed to UV light, where the uncovered resist undergoes a chemical change. The resist is then developed in a remover solution, exposing the electrode patterns on the chip, while the rest of the chip remains covered in resist.

With the electrode patterns prepared, we deposit metal using thermal evaporation, as shown in Fig. 3.3(b). We first deposit a 5 nm sticking layer of Cr to help the Al adhere to the  $\text{SiO}_2$ , followed by a 30 nm layer of Al over the entire chip. After the evaporation is completed, metal lift-off is performed by soaking the chip in a warm acetone bath to remove the resist and excess metal and leave the desired Al electrodes.

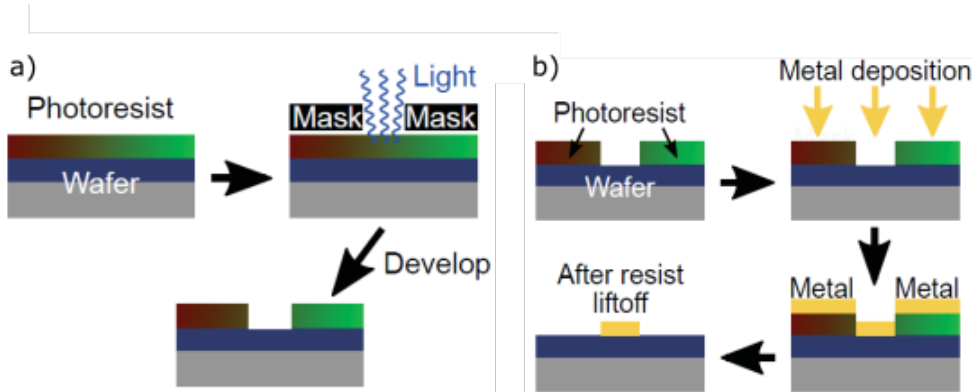


Figure 3.3: Photolithography and deposition of aluminium electrodes. (a) Photoresist is spun onto the Si chip with the hBN trench. A photomask patterns the incident UV radiation. The resist is then developed, exposing the  $\text{SiO}_2/\text{Si}$  where the electrodes will be deposited. (b) 5 nm of chromium are deposited onto the developed photolithography pattern as a sticking layer, followed by 30 nm of aluminium. After lift-off, the  $\text{SiO}_2/\text{Si}$  is coated in an Al electrode pattern.

### 3.2.2 Suspending bilayer graphene over the aluminium mirror

With the Al electrodes in place, we complete our optical cavity by suspending a bilayer graphene crystal above the backplane of Al. We follow the deterministic transfer method presented in Chapter 2. Figure 3.4 shows the before (a) and after (b) of Device WWA12, which was our first successful BLG/air/Al cavity. The length of the

suspension was  $L = 6.2\mu\text{m}$ . A shorter suspension length would decrease the number of measurement points on our optical cavity due to our laser spot size ( $\approx 1\mu\text{m}$ ). Also seen in Fig. 3.4(b) is a graphite contact, which was used to repair a gap in the Al electrode on top of the hBN.

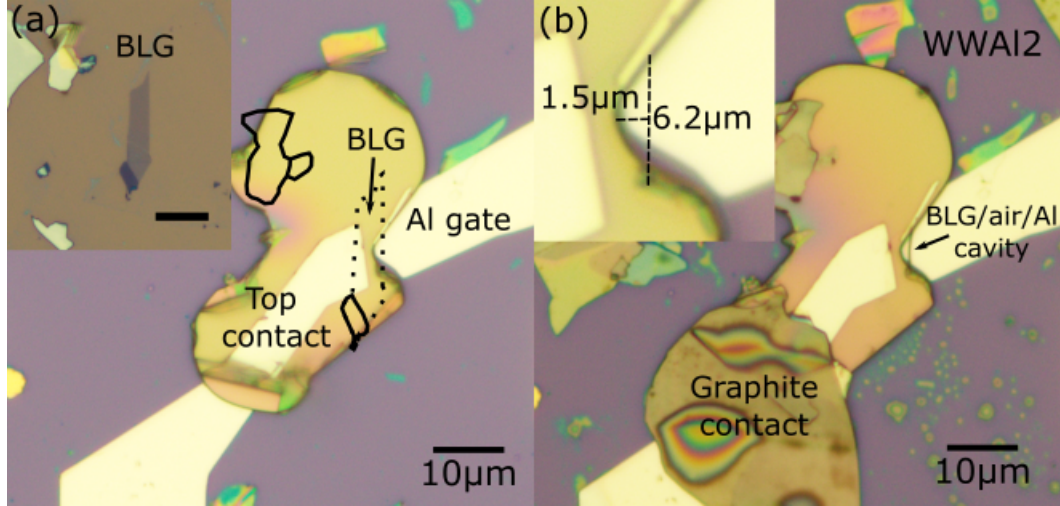


Figure 3.4: Before and after suspension of bilayer graphene over aluminium to form an optical cavity. (a) Suspension plan for Device WWA12 showing a trace of the bilayer graphene flake to be used (inset,  $4\mu\text{m}$  scale bar). (b) Completed suspension of Device WWA12 where the edge of the suspended graphene is clearly visible over the Al. A graphite flake has been used to repair a break in the top Al contact (connected to ground in order to apply a voltage to the BLG). (Inset) The suspended length is  $L = 6.2\mu\text{m}$  with a width of  $1.5\mu\text{m}$ .

### 3.2.3 Opto-electronic measurement instrumentation

For our optical measurements, we use a Renishaw inVia Raman spectrometer equipped with a Prior ProScan motorized translation stage, an Innovative Photonic Solutions 532 nm spectrum stabilized laser source (model I0532SR0050B), and a Leica DM LM optical microscope, as shown in Fig. 3.5(a). The translation stage has a spatial precision of  $0.05\mu\text{m}$  in the in-plane X and Y directions (Fig. 3.5(b)), according to specifications. Renishaw's WiRE software controls the translation stage and has many customizable acquisition options, including acquisition time laser power, mapping dimensions, and automatic laser focusing. The holographic filters fulfill the same function as a dichroic mirror, directing the excitation laser beam

toward the sample, and allowing the scattered light to pass through it toward the diffraction grating and CCD camera.

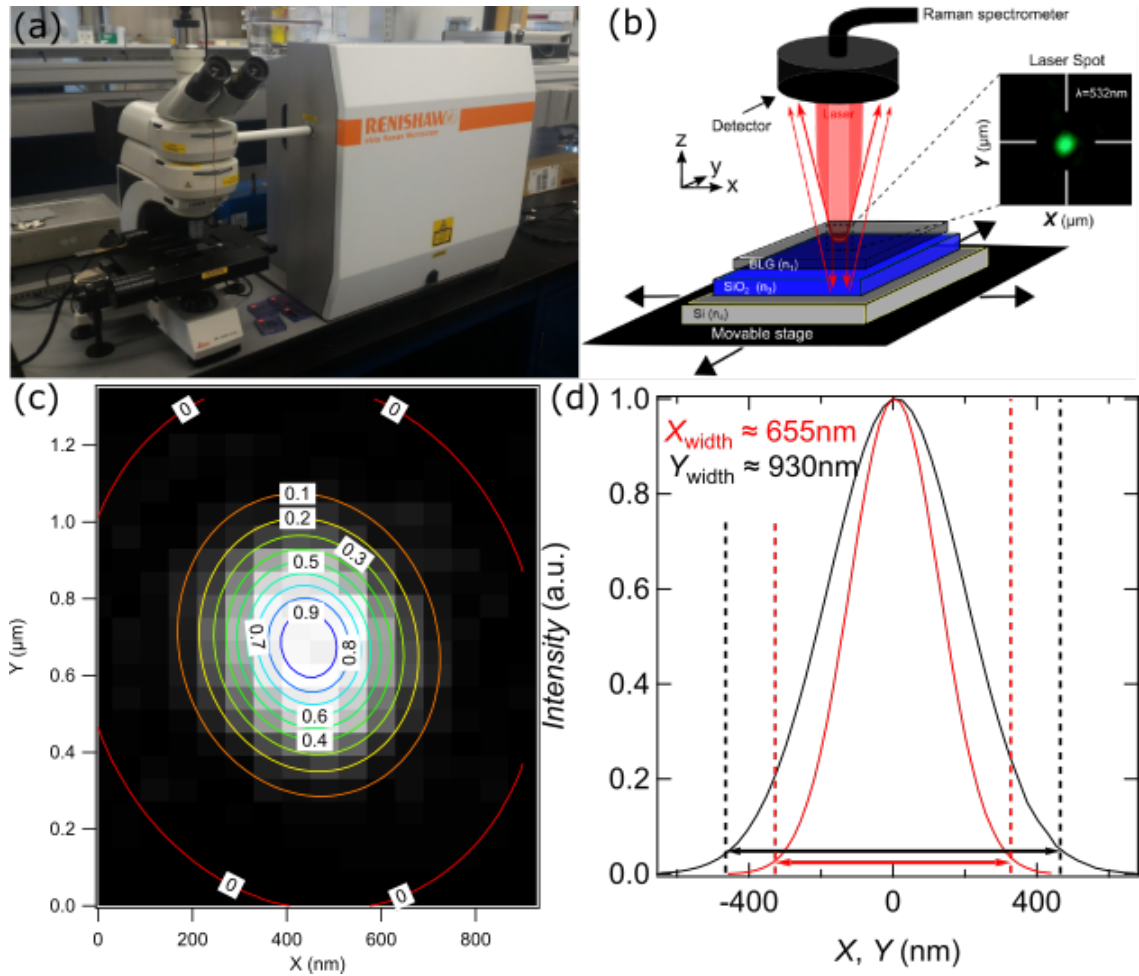


Figure 3.5: Opto-electronic instrumentation to study light-matter interactions. (a) Renishaw inVia Raman spectrometer system with Leica optical microscope and Prior Scientific XYZ translation stage. Figure modified from [62]. (b) Schematic of the Raman spectrometer and microscope translation stage. A laser with wavelength 532 nm is normally incident to the sample and Raman scattered light is collected by a detector. Also, an optical image of the laser spot. Figure reproduced from [26]. (c) Plot of greyscale intensity for each pixel on the optical image of our laser spot with the overlying 2D Gaussian fit. (d) Line-cuts of our 2D Gaussian fit in the x and y directions, showing the widths of our laser spot.

The 100x objective used in our measurements produces an elliptical laser spot, as seen in Fig. 3.5b. To characterize our laser spot, we first focus it on a Si substrate and capture an image with the highest possible acquisition time such that the spot is clearly visible but not saturated. We then convert the image to greyscale, where

the value of each pixel represents a measure of intensity. Once this data is plotted in Igor Pro 7, we fit the intensity profile to a 2D Gaussian function:

$$f(x, y) = A * \exp(-(a(x - x_0)^2 + 2b(x - x_0)(y - y_0) + c(y - y_0)^2)) \quad (3.1)$$

with coefficients  $a = \frac{\cos^2(\theta)}{2\sigma_x^2} + \frac{\sin^2(\theta)}{2\sigma_y^2}$ ,  $b = \frac{-\sin^2(2\theta)}{4\sigma_x^2} + \frac{\sin^2(2\theta)}{4\sigma_y^2}$ , and  $c = \frac{\sin^2(\theta)}{2\sigma_x^2} + \frac{\cos^2(\theta)}{2\sigma_y^2}$ .  $A$  is the amplitude,  $\sigma_{x,y}$  are the widths in the x and y directions, and  $\theta$  is the rotation of the Gaussian spot. The results of this fit are shown in Fig. 3.5(c). Integrating in the x and y directions, we see that 99% of our laser power rests in  $X_{width} = 655nm$  and  $Y_{width} = 930nm$ , as seen in Fig. 3.5(d).

### 3.3 Measurement of Raman factor for a BLG/air/Al optical cavity

We first capture Raman data for our BLG suspended over Al with no gate voltage applied ( $V_g = 0$ ). Our first successful suspension over Al was named Device WWAl2, which is presented again in Fig. 3.6(a). There we define the X and Y scanning axes along which our measurements were performed. A schematic side-view of this device can be seen in Fig. 3.6(b), showing part of the BLG laying on the top Al contact (needed to apply a voltage on the graphene flake). We first present the measurement procedures (reduction of uncertainty due to microscope stage drift) and data analysis (eliminating a Raman signal from fabrication residues) which were performed in this section, before presenting and discussing the Raman data in Section 3.4. We demonstrate that Raman factor can be tuned 1.8x over a 10 nm change of  $h_{air}$  in the same device.

#### 3.3.1 Reducing spatial uncertainty due to microscope stage drift

The measurements which were performed on WWAl2 are summarized in Fig. 3.1. Each measurement represents a line scan in the X or Y direction, which spans the entire respective range of these axes, presented in Fig. 3.6a (except for scans Y1 and

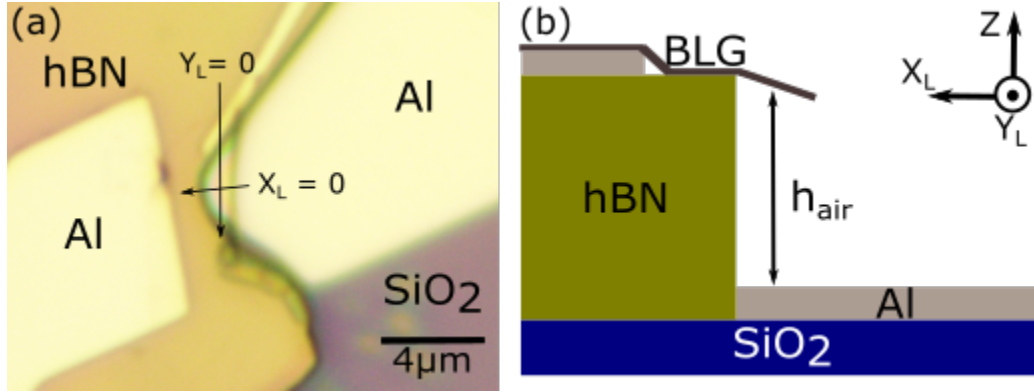


Figure 3.6: Definition of axes for Raman line scans on Device WWA12. (a) Optical image of Device WWA12 defining the  $X_L$  and  $Y_L$  laser positions used in our measurements. (b) Schematic side-view of our device showing the BLG in contact with the top Al electrode and suspended over the bottom Al electrode.

Y2). Laser powers were measured before and after each scan, with the average value being used in the subsequent data analysis. Before and after images of a predefined origin near the device confirmed that the (x,y) position of the laser did not drift significantly over the course of a measurement. Images of the defined line scans were taken before each run with no change in the scan positions. The length scales of images taken with our Raman microscope agree with those taken by multiple image sources in our laboratory, as seen in Fig. 3.7.

Initially, the laser spot was only focused on the suspended BLG before each line scan, which produced the data seen in Fig. 3.8(a). It was later found that refocusing the laser spot for each data point reduced spatial uncertainty in the Z direction (likely due to motor stage drift), producing the cleaner data shown in Fig. 3.8(b). Focusing the laser spot ensured that laser power was distributed over the smallest possible area on our device, limiting unwanted features.

### 3.3.2 Raman signal from microfabrication residues

Over the course of our measurements, we noticed an unexpected Raman peak appearing near graphene's 2D peak, as seen in Fig. 3.9(a). When fitting graphene's 2D peak, this unexpected peak effectively raised the baseline of our fit, reducing the area (counts) of the 2D peak. We attribute this peak to fabrication residues,

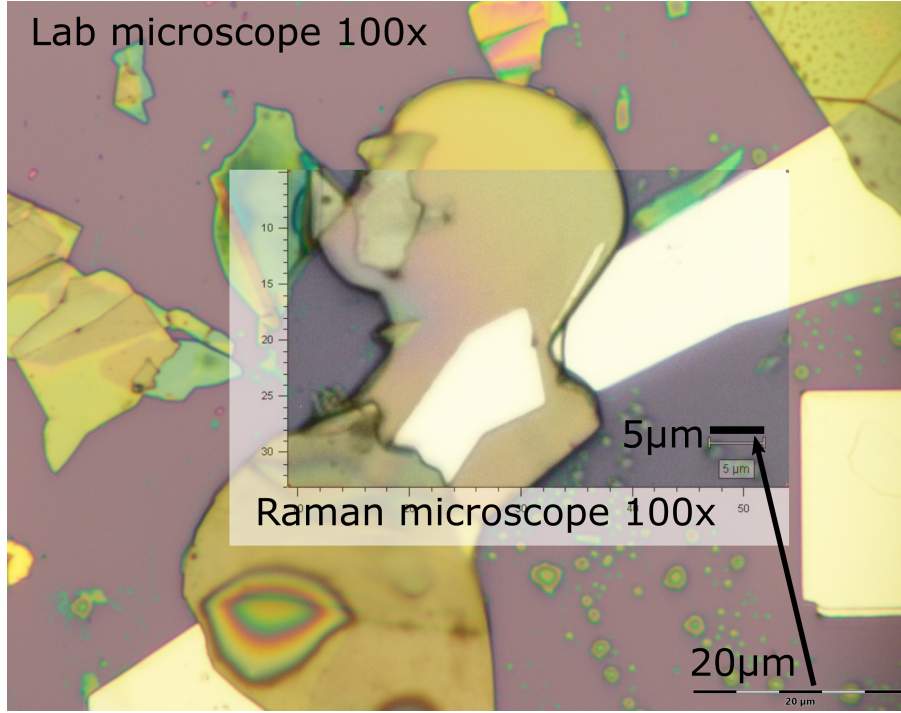


Figure 3.7: Comparison of length scales. The length scale of images taken with our Raman microscope using a 100x objective correspond to those taken using another microscope in our lab with a different 100x objective.

Device name: WWA12				
Scan direction	Scan datasets	Step size ( $\mu\text{m}$ )	Laser power min-max ( $\mu\text{W}$ )	Refocus
X	ScanX(1-3)	0.3	944-967	No
"	ScanX(4-5)	0.2	962-965	No
"	ScanX(6-8)	0.1	919-954	No
"	ScanX(9-11)	0.1	885-930	Yes
Y	ScanY(1-2)	0.1	948-974	Yes
"	ScanY(3-5)	0.5	965-974	Yes
"	ScanY(6-7)	0.1	903-937	Yes

Table 3.1: List of line scans performed in the X and Y directions on Device WWA12. All scans except for ScanY1-2 were performed over the entire respective range of  $X_L$  and  $Y_L$  as shown in Fig. 3.6. Laser powers were measured before and after each scan, with the min and max values of each subset recorded above. We began to manually refocus the laser at every  $X_L - Y_L$  location along the scan beginning with ScanX9.

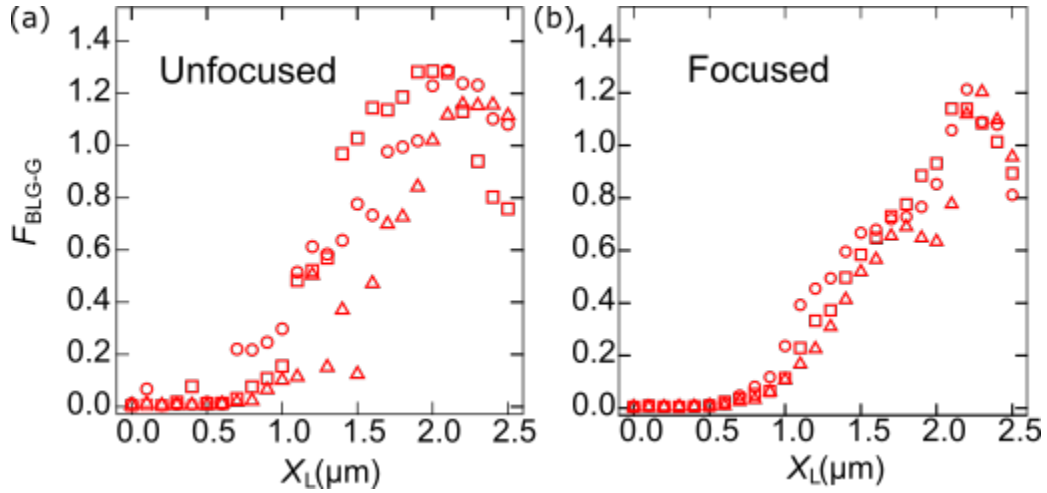


Figure 3.8: Reducing spatial uncertainty due to drift in the Z-direction. G-peak Raman factor data before (a, X6-X8) and after (b, X9-X11) we focused the laser spot for each measurement point. Focusing the laser for each point reduced noise by ensuring that laser power was distributed over the smallest possible area.

as measurements could not confirm exactly which material (aluminium, aluminium oxide, acetone, etc.) was at cause. It must also be noted that graphene has a small  $G^*$  peak in this same range, as seen in Fig. 3.9(b) [63]. To remove any effect of these residues on our data analysis, we extended the fit range of our 2D peak and added the residue and  $G^*$  peaks to our fit function, as seen in Fig. 3.9(c). The residue peak was fit with a Lorentzian and a Gaussian, while the  $G^*$  peak was fit with two Gaussians. Finally, we subtracted the fitted residue and  $G^*$  peaks from our data before performing a final fit on the graphene 2D peak. This procedure eliminated  $\approx 5\%$  error from our analysis, as presented in Fig. 3.9d.

### 3.4 Experimental Raman factor vs theoretical model

After the pre-processing steps outlined in Section 3.3, our data are ready for analysis. We first measure the height of the optical cavity to model theoretically the data. AFM traces taken before the deposition of Al for Device WWA12 show that the supporting hBN has a height of  $(660 \pm 10)$  nm, as seen in Fig. 3.10(a). After subtracting the  $(35 \pm 5)$  nm of Cr and Al deposited at the bottom of the cavity, this gives an initial cavity height of  $(625 \pm 10)$  nm, as shown in Fig. 3.10(b). Our Raman factor model

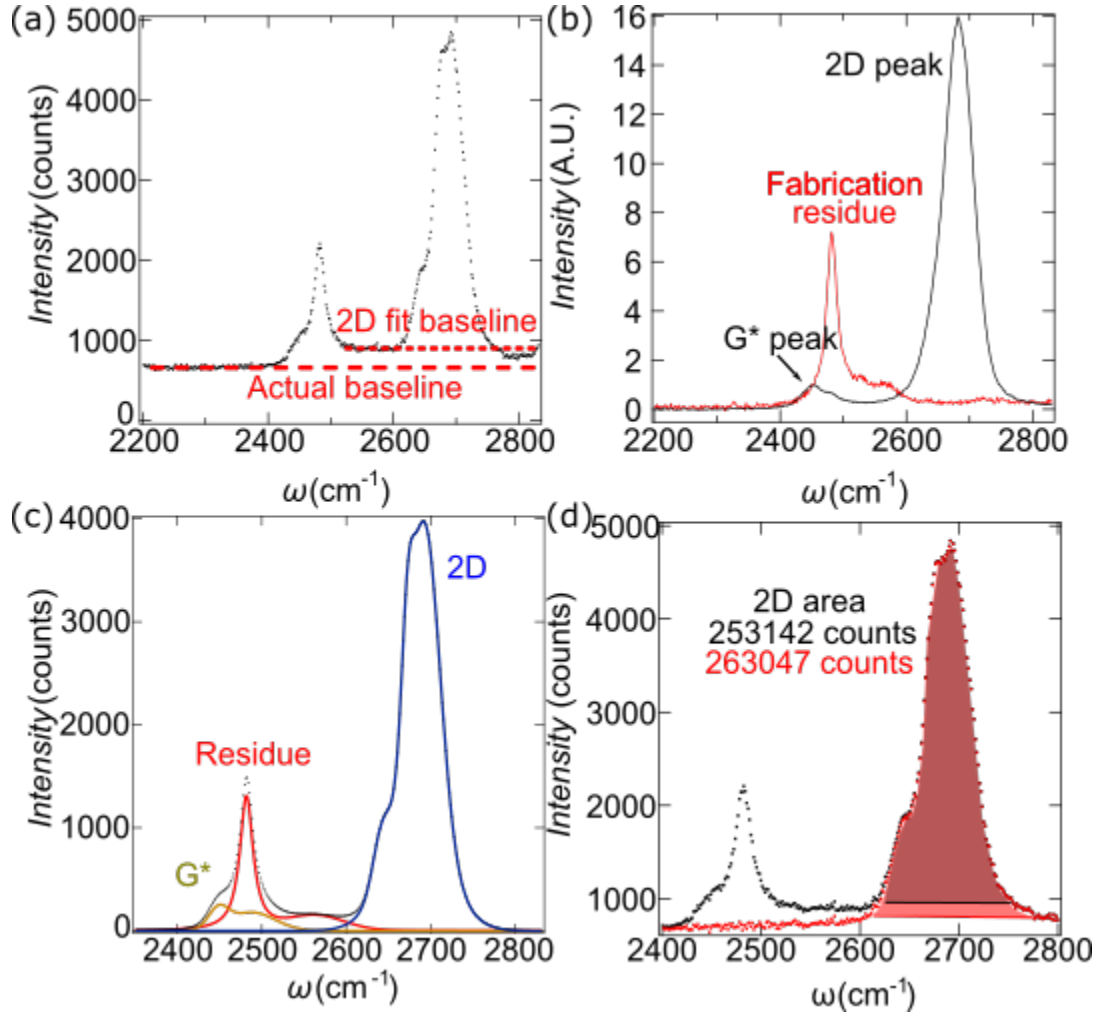


Figure 3.9: Eliminating spurious Raman counts due to fabrication residue. (a) Example of Raman data showing a peak at  $\approx 2480 \text{ cm}^{-1}$  (left). This peak affects the baseline fit of our 2D peak (right), producing a baseline that is higher (fit baseline) than the actual baseline of our data. (b) Raman data showing that the peak is a combination of two peaks: the  $G^*$  peak ( $\approx 2450 \text{ cm}^{-1}$ ) from graphene (black) and a peak that we attribute to fabrication residues (red). Raman data (black) whose fit includes the  $G^*$  (gold) and 2D (blue) peaks of bilayer graphene, as well as the that of residue peak (red). (d) Raman data before (black) and after (red) subtracting the  $G^*$  and residue peaks, allowing for a better estimate of the area under the 2D peak.

predicts that  $F_{2D}$  produces a minor beat resonance near this particular cavity height, which lies between two primary maxima, as seen in Fig. 3.10c. However, the imperfect quality of our device means that the signal-to-noise ratio of this minor feature will not be resolvable with changing cavity height, and that we can only expect  $F_{2D}$  to lie somewhere between 0 – 0.67.

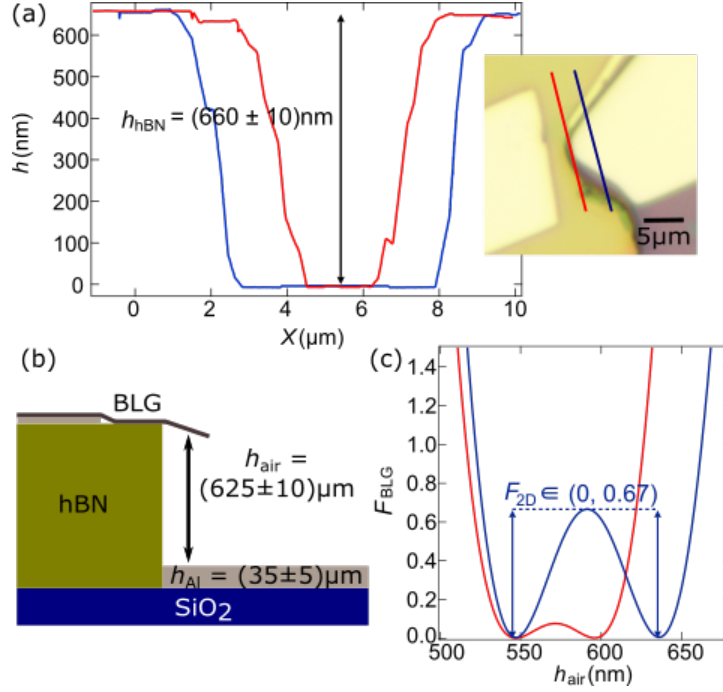


Figure 3.10: Cavity height and Raman factor model for Device WWAL2. (a) hBN cavity height for the AFM trace positions indicated in the inset, taken before the deposition of Al. The cavity height is estimated to be  $(660 \pm 10)$  nm. (b) Schematic side view of Device WWAL2. After considering the Cr/Al mirror  $(35 \pm 5)$  nm, the optical cavity height is estimated to be  $(625 \pm 10)$  nm. (c) Raman factor model for Device WWAL2 near the optical cavity height. The predicted beat resonance of the 2D peak Raman factor,  $F_{2D}$ , is a feature that we do not expect to capture with changing height, though our measurements should fall within the resonance range.

Our first measurements of Device WWAL2, with  $V_g = 0$  and with line scans in the X direction, are shown in Fig. 3.11(a). The highest quality data was captured when refocusing the laser spot at each  $X_L$  position, with step sizes of  $0.1 \mu\text{m}$  (Scans X9-X11). The measured G peak Raman factors,  $F_G$ , can be seen in Fig. 3.11(b). The green data point at  $X_L = 1.5 \mu\text{m}$  corresponds to the laser position shown in Fig. 3.11(a). Figure 3.11(c) shows the averaged  $F_G$  (3 scans: X9, X10, X11) and that predicted by our model (solid line). We see an excellent agreement between data and model. As

our scan approached the hBN,  $F_G$  approaches the theoretical value for the measured cavity height,  $(625 \pm 10)$  nm. The estimated slack of  $\approx 10$  nm is comparable to that of  $5\mu\text{m}$ -diameter graphene drums [64]. The error bars shown result from the uncertainty on the thickness of our  $\text{SiO}_2$  (5%), which affects our Raman factor calibration, and the uncertainty on our laser power (2%). We also show that  $F_G$  can be tuned 1.8 folds over a 10 nm change in air spacer thickness when suspended over Al. The inset of Fig. 3.11(c) presents the calculated  $A_{BLG}$  for BLG/air/Al optical cavities, where our device possesses an exclusive light absorption as high as 15.6%, 3.4 times that of BLG in vacuum. The calculated  $F_{2D}$  data is shown in Fig. 3.11(d), where the values fall within the expected range of  $(0, 0.67)$ .

The next measurements were performed with line scans in the  $Y_L$  direction, as shown in Fig. 3.12(a). Again, the best data was taken by refocusing the laser spot after each  $0.1\mu\text{m}$  step. We show our laser spot at the  $Y_L = 4.2\mu\text{m}$  position in Fig. 3.12(a). Figure 3.12(b) shows the calculated  $F_G$  for given optical cavity heights (black curve) overlaid on the measured  $F_G$  (red circles). We see the minor slacking of the graphene flake in the centre of the optical cavity (top axis shows  $h_{air}$ ). The minimum estimated optical cavity height of  $\approx 613$  nm is similar to that found at the equivalent X position ( $X_L = 1.1\mu\text{m}$ ),  $\approx 614$  nm.

Confident in our ability to both model and measure Raman factor for our optical cavity with a backplane Al mirror, we proceed to examine the in-situ tunability of Raman factor with an applied voltage.  $F_G$  was tuned 3.8 folds over a 100 nm change in air spacer thickness when suspended over  $\text{SiO}_2$  (Fig. 2.14(b)). Over Al,  $F_G$  was tuned 1.8 folds over 1/10 of the change in  $h_{air}$ . With further control of  $h_{air}$  via electrostatic gate tuning, we believe we can reach  $\Delta F/F \gg 10$  in a single device.

### 3.5 Gate voltage tunability of light-matter interactions in graphene

In Section 3.4, we demonstrated that we can fabricate BLG/air/Al optical cavities, as well as model and measure the Raman factor which quantifies the scattering of light inside the BLG. We showed that  $F_G$  can be tuned 19 folds in Raman measurements of BLG/hBN/Al optical cavities (50 nm change in  $h_{hBN}$ ) and that it can be tuned 1.8 folds in a single BLG/air/Al optical cavity (10 nm change in  $h_{air}$ ). We believe

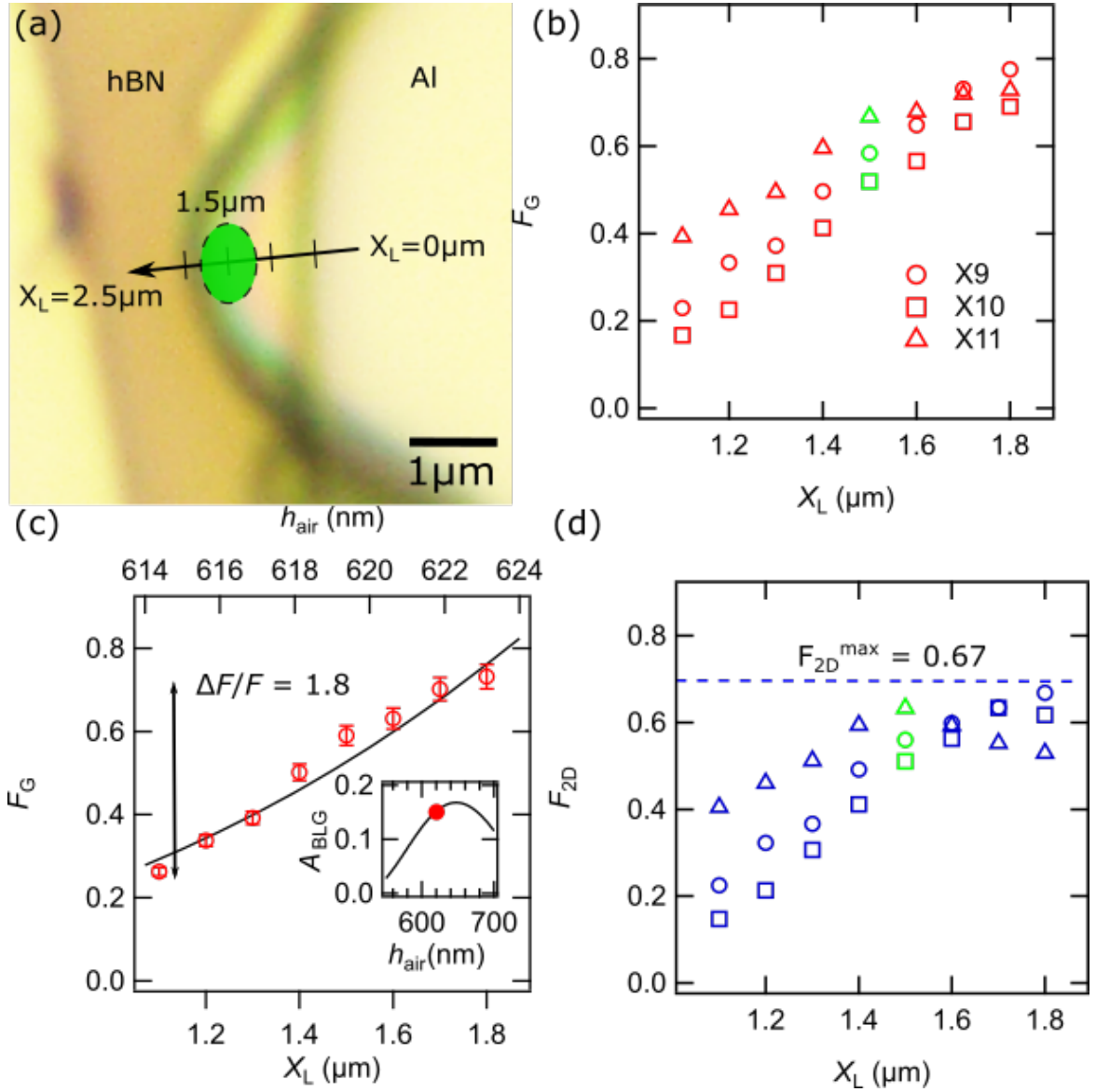


Figure 3.11: Raman factor data for the X direction of Device WWA12. (a) Optical image of Device WWA12 showing the defined X positions, as well as a depiction of our laser spot at  $X_L = 1.5 \mu\text{m}$  (green data in (b)). (b) Calculated G peak Raman factor,  $F_G$ , for optical cavity laser positions. (c) Modelled  $F_G$  (black) corresponding to optical cavity height (top) fitted to our averaged  $F_G$  data (red, bottom), showing the evolution of optical cavity height. Our data estimates a slack of 10 nm with optical cavity height increasing to that predicted by AFM ( $625 \pm 10$  nm) as the laser position approaches the hBN.  $F_G$  was tuned 1.8 folds over the 10 nm change in cavity thickness. The inset shows a modelled exclusive light absorption of 15.6% for our device, 3.4 times that of BLG in vacuum. (d) Calculated 2D peak Raman factor,  $F_{2D}$ , for optical cavity laser positions. The values fall within the expected range of (0, 0.67) predicted by our model.

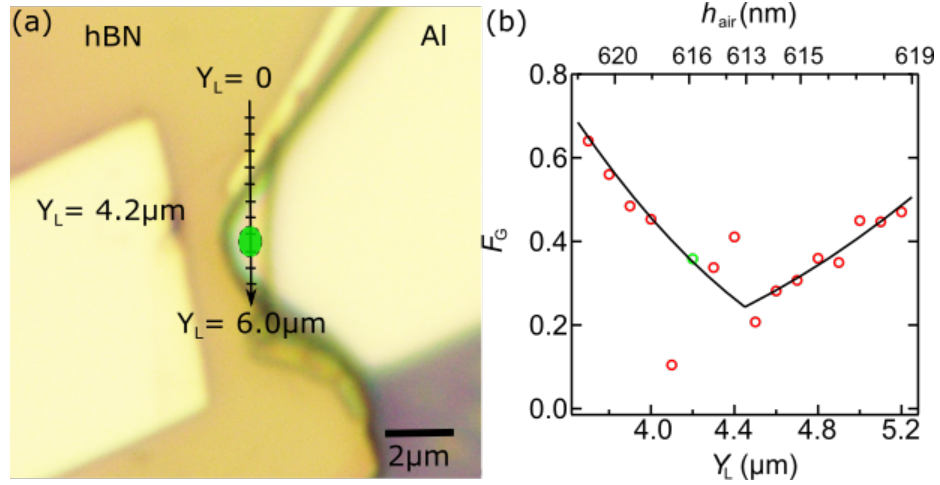


Figure 3.12: Raman factor data for the Y direction of Device WWA12. (a) Optical image of Device WWA12 showing the defined Y positions, as well as a depiction of our laser spot at  $Y_L = 4.2 \mu\text{m}$  (green data in (b)). (b) Modelled  $F_G$  (black) corresponding to optical cavity height (top) fitted to our  $F_G$  data (red, bottom), showing the evolution of optical cavity height. We observe the slack of our BLG flake in the centre of the optical cavity.

that further control of  $h_{air}$  via electrostatic gate tuning will allow for much greater tunability, and consequentially much greater on/off ratios, in a single device.

In this section, we add the electrostatic deflection of graphene to our Raman factor model in order to predict the *in-situ* tunability which can be achieved in future BLG/air/Al optical cavities. Next, we present the packaging of Device WWA12 and the instrumentation used for electro-optical measurements. Finally, we show that Raman factor can be tuned *in-situ* by 20% and  $h_{air}$  by 3 nm with the application of  $V_g = 500$  mV.

### 3.5.1 Tuning optical cavity thickness with $V_g$

In order to tune both the Raman factor, and the underlying exclusive light absorption, in our graphene devices *in-situ*, we must tune the thickness of the air medium ( $h_{air}$ ) between the graphene flake and the aluminium mirror. This can be achieved by applying an electrostatic force with a gate voltage,  $V_g$ , as seen in Fig. 3.13, to deflect the flake towards the mirror. Taking the height ( $h_{hBN}$ ) of the supporting hBN medium as the origin, the deflection of the midpoint of the graphene flake,  $h_0$ , can be expressed as [65]:

$$\frac{C_g^2 V_g^2 L^2}{2\epsilon_0} = 8T_0 t h_0 + \frac{64}{3} \frac{Y t}{1 - \nu^2} \frac{h_0^3}{L^2} \quad (3.2)$$

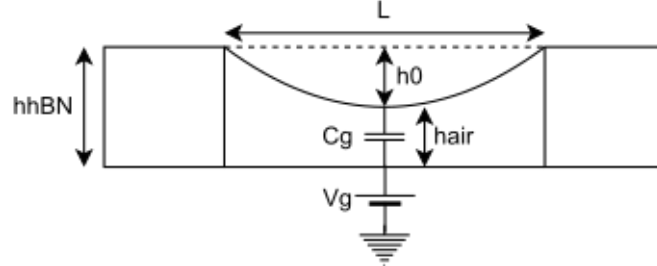


Figure 3.13: Electrostatic deflection of a suspended graphene NOEMS. The capacitance,  $C_g$  between the bottom Al electrode and the suspended graphene flake creates an electrostatic force when  $V_g$  is applied. This force deflects the flake, increasing  $h_0$ , and decreases the thickness of the optical cavity,  $h_{air}$ .

Here  $C_g$  is the gate capacitance per unit area,  $L$  is the suspension length, and  $T_0 = [Y/(1 - \nu^2)](\Delta L/L)$  is the pre-existing stress in the membrane with relative elongation  $\Delta L$ , which sets the initial deflection at  $V_g = 0$ .  $\epsilon_0$  is the vacuum permittivity,  $t$  is the thickness of the graphene (0.34 nm per layer),  $Y$  is the Young's Modulus of graphene (1 TPa), and  $\nu$  is the Poisson ratio (0.165).

When considering the capacitance of the graphene, one of the most common approximations is to assume that the flake is parallel to the underlying gate [43,65,66]. While the device that we are fabricating possesses a single dielectric (air), most graphene electromechanical systems are suspended above  $\text{SiO}_2$ , where both media must be taken into account (considered in order to verify our accuracy with published data):

$$C_{air}^{parallel} = \frac{\epsilon_0}{h_{air}} \quad (3.3a)$$

$$C_{SiO_2} = \frac{\epsilon_{SiO_2} \epsilon_0}{h_{SiO_2}} \quad (3.3b)$$

where  $h_{air} = h_{hBN} - h_0$ .

When added in series the total capacitance can be expressed as:

$$C_g^{parallel} = \frac{\epsilon_{SiO_2} \epsilon_0}{\epsilon_{SiO_2} h_{air} + h_{SiO_2}} \quad (3.4)$$

One can improve on the parallel plate model by assuming that the flake forms a

parabola over its suspended length with its vertex located at the deflected distance,  $h_0$ . This changes the capacitance of the air layer to [65],

$$C_{air}^{parabola} = \frac{\epsilon_0}{\sqrt{h_0(h_{air} - h_0)}} \arctan\left(\sqrt{\frac{h_0}{h_{air} - h_0}}\right) \quad (3.5)$$

which gives a total capacitance of:

$$C_g^{parabola} = \left\{ \frac{\sqrt{h_0(h_{air} - h_0)}}{\epsilon_0} \left[ \arctan\left(\sqrt{\frac{h_0}{h_{air} - h_0}}\right) \right]^{-1} + \frac{h_{SiO_2}}{\epsilon_{SiO_2}\epsilon_0} \right\}^{-1} \quad (3.6)$$

Since the diameter of the laser spot used for our measurements is on the same order as the width of our devices ( $\approx 1\mu\text{m}$ ), it is best to consider an average deflection,  $\bar{h}$ , when determining the thickness of air, as opposed to  $h_0$ . Assuming that the graphene has a parabolic shape, the deflection over  $-L/2 \leq x \leq L/2$  can be expressed as:

$$h(x) = h_0 \left( 1 - \frac{4x^2}{L^2} \right) \quad (3.7)$$

Taking the average of this function gives  $\bar{h} = 2h_0/3$ .

Figure 3.14 is a reproduction (solid curves) of simulations from [65] (markers) and demonstrates that the standard parallel plate assumption is valid for ( $V_g < 10V$ ) for the reported devices. An even better approximation is that the parallel plate is located at the average deflection height (black curve), which matches the parabolic curve for ( $V_g < 25V$ ).

### 3.5.2 Tuning Raman factor *in-situ* with $V_g$

Using our theoretical knowledge we can calculate the expected tunability of Raman factor via an applied voltage. Here we use Equation 3.2 to solve for  $h_{air}$ , which is subsequently plugged into our Raman factor equations where appropriate. For computational ease we approximate  $C_g$  using the parallel plate approximation at the average deflection,  $\bar{h}$ , since we expect  $V_g \leq 20V$ .

We simulated the deflection (Fig. 3.15(a)) and Raman factor (Fig. 3.15(b)) of BLG as a function of  $V_g$  for relative elongations of  $\Delta L = -1, 0, 1$  nm for the optical cavity seen in the inset of Fig. 3.15(a). This particular u-shaped hBN cavity (to be used in future devices) allows for a suspension length of  $L = 7.2\mu\text{m}$  for a width

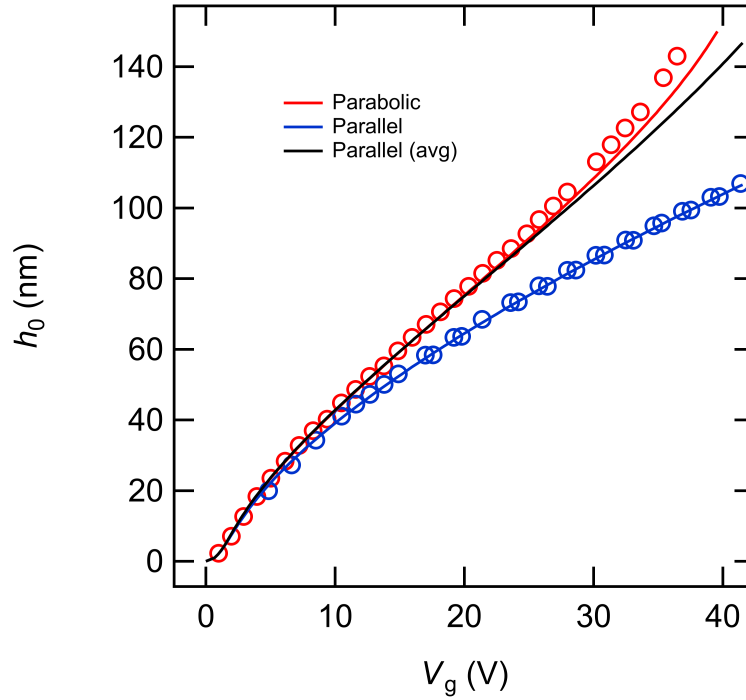


Figure 3.14: Modelling graphene deflection with different capacitor geometries. Proof of concept taken from [65], demonstrating the ability to reproduce Eq.3.2 with both parallel plate (blue, Eq.3.4) and parabolic flake (red, Eq.3.6) capacitances. Assuming a parallel plate geometry at the average deflection height (black) of the graphene flake is equivalent to a parabolic flake for  $(V_g < 25V)$ .

of  $W = 2\mu\text{m}$  and has an average cavity height of  $h_{air} = h_{hBN} - h_{Al} = 293\text{ nm}$ . Notably, with this cavity geometry, our model predicts that Raman factor can be suppressed down to 0 and enhanced up to 15 by applying 15 V, giving an on/off ratio of  $\approx 33000$  and making it a perfect platform to demonstrate the tunability of light-matter interactions over orders of magnitude.

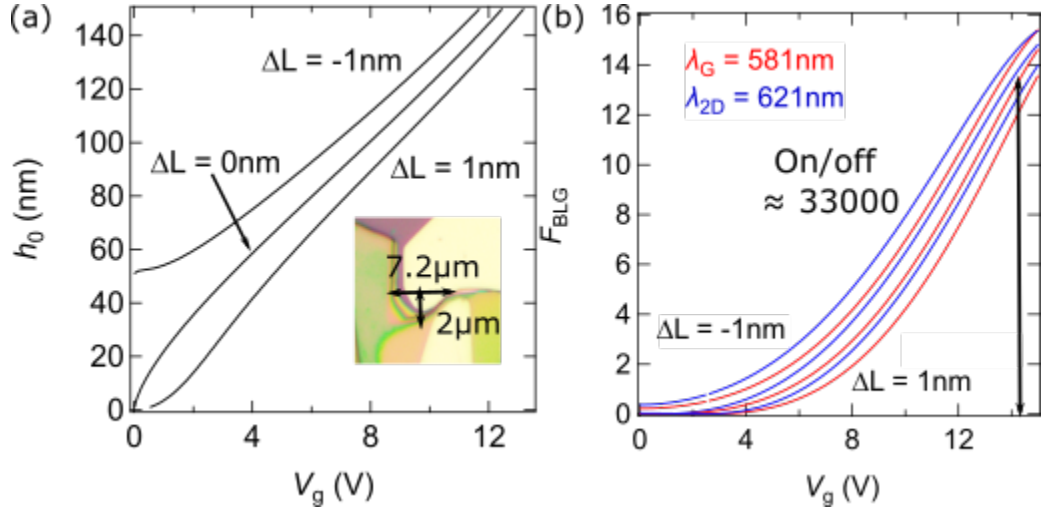


Figure 3.15: Calculated Raman factor as a function of  $V_g$  for Device WWA11. (a) Optical image of a bilayer graphene flake on  $\text{SiO}_2$  before suspension. (b) Suspension plan of WWA11 showing an optical image of the hBN trench with a trace of the bilayer graphene flake overlaid. This particular cavity would have been tilted due to a height difference across the trench. (c) Model of the graphene deflection ( $h_0$ ) with increasing applied voltage ( $V_g$ ) for given relative elongations ( $\Delta L$ ), setting the initial slack of the BLG. (d) Corresponding Raman factor ( $F_{BLG}$ ) model with increasing applied voltage predicting an increase from 0 to 15 for both the G peak (red) and 2D peak (blue) at 15 V and on/off ratios as high as 33000.

### 3.5.3 Device packaging and instrumentation for electro-optical measurements

In order to apply a gate voltage to our BLG flake and tune the Raman factor, we must connect the optical cavity to an electrical circuit. We do so by inserting the Si chip holding our optical cavity into a chip carrier and adding wirebonds that connect our Al contacts to the chip carrier's pins, a process that is summarized in Fig. 3.16. The Si chip is first glued to a chip carrier using silver paint, as seen in Fig. 3.16(a). Next, we wirebond the Al contacts of our device (connected to large contact pads for

bonding) to the pins of the chip carrier; an example chip with gold contact pads is seen in Fig. 3.16(b). Figure 3.16(c) shows a closer view of the wirebonds while Fig. 3.16(d) shows a tiled SEM image of the bonding pads.

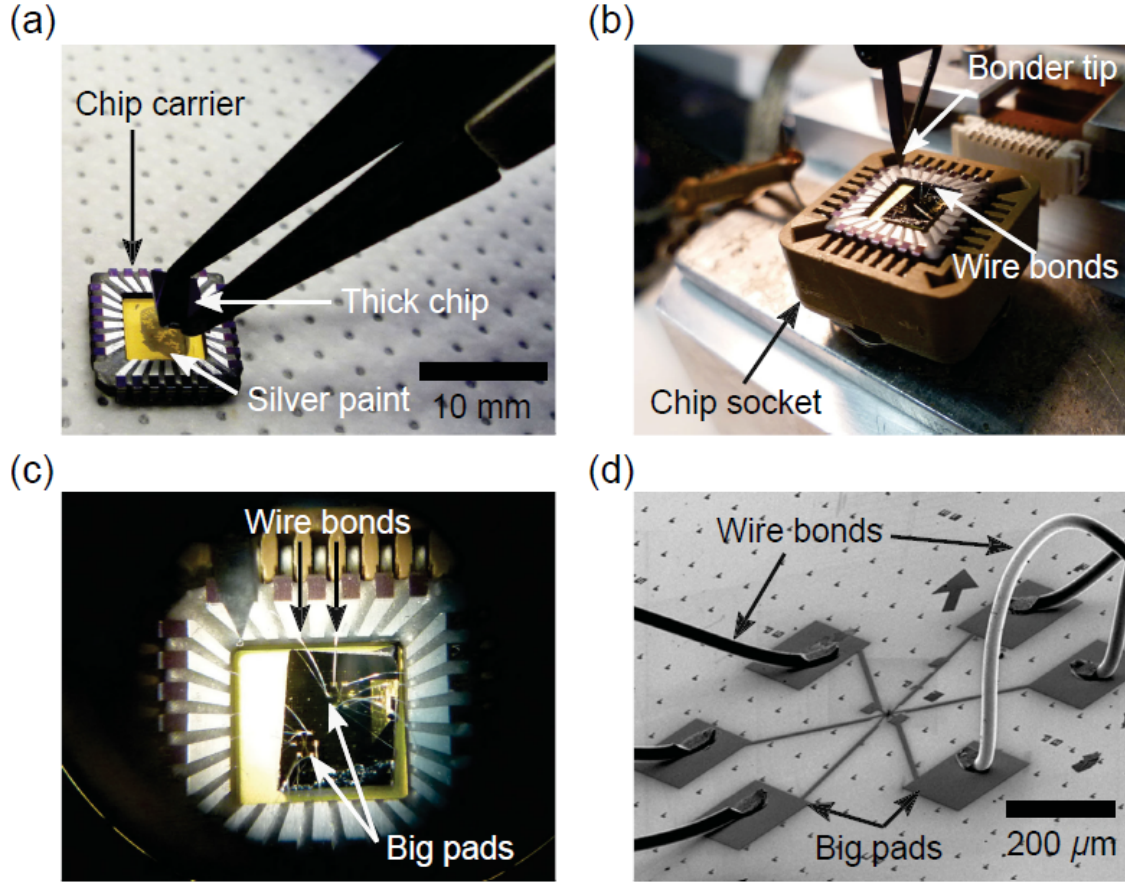


Figure 3.16: Preparing the optical cavities for opto-electronic measurements. (a) The Si chip containing the optical cavity is glued to a chip carrier using silver paint. (b) The chip carrier is placed in a grounded chip socket for wire bonding. (c) A closer view of the Si chip with wire bonds extending from the chip carrier to the electrode bonding pads. (d) Tilted SEM image of wire bonds attached to a six-point pattern. Figure reproduced from [51].

Once wirebonded, we can place our chip carrier in a custom sample holder which fits into our Raman microscope stage, as seen in Fig. 3.17(a). The working distance of our 100x objective is large enough that the protruding wirebonds will not touch the objective. Flexible SMA-to-BNC wires connect to our sample holder so as to not impede the movement of the microscope stage. The simple electrical circuit used to apply  $V_g$  to our BLG is shown in Fig. 3.17(b). We use a Keithley 2400 sourcemeter as our voltage source with a low pass filter and  $1M\Omega$  limiting resistor in series to

clean our signal and prevent current overloads, respectively.

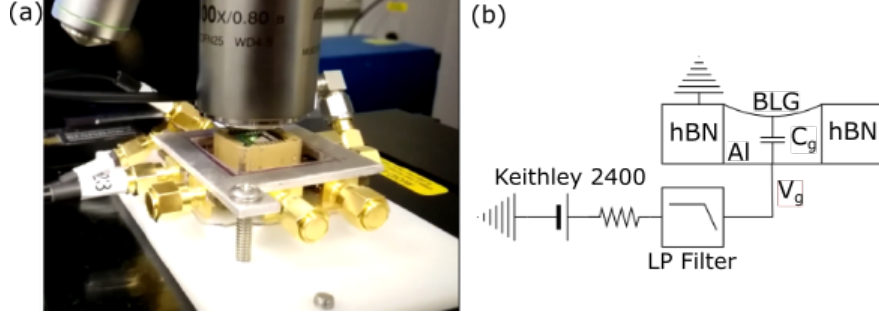


Figure 3.17: Electro-optical instrumentation. (a) Optical cavity mounted to our room temperature sample holder. Flexible SMA-to-BNC wires impede the movement of the microscope stage as little as possible. Figure modified from [62]. (b) Schematic of the electrical circuit used to apply a voltage to the graphene (Gr).

### 3.5.4 Measurement of Raman factor vs gate voltage

The geometry of Device WWA12 was slightly altered during the wirebonding process due to electrostatics, as can be seen in Fig. 3.18(a). The suspension length and suspended area were reduced from the initial device state, as indicated by the dashed line, leaving little room for measurement. We were, however, able to apply gate voltages up to 500 mV before the collapse of our cavity; the measured  $F_G$  data can be seen in Fig. 3.18(b). It must be remembered that increasing gate voltage would deflect the BLG towards the Al mirror, reducing the cavity height. By modelling  $F_G$  theoretically, we estimate that the wirebonding process deflected our BLG  $> 100$  nm downwards. Despite the small gate voltages applied, we clearly observe an increasing  $F_G$  with gate voltage, corresponding to an electrostatic deflection of  $\approx 3$  nm, according to our model.  $F_g$  is tuned by 20% over this small change in air spacer thickness. These results show that light-matter interactions can indeed be tuned *in-situ* with  $V_g$ , and accurately modeled by calculating Raman factor. We hope to reproduce these findings in the future and extend the applied  $V_g$  to achieve higher tunability and on/off ratios at realistic voltages, as demonstrated in Section 3.5.2.

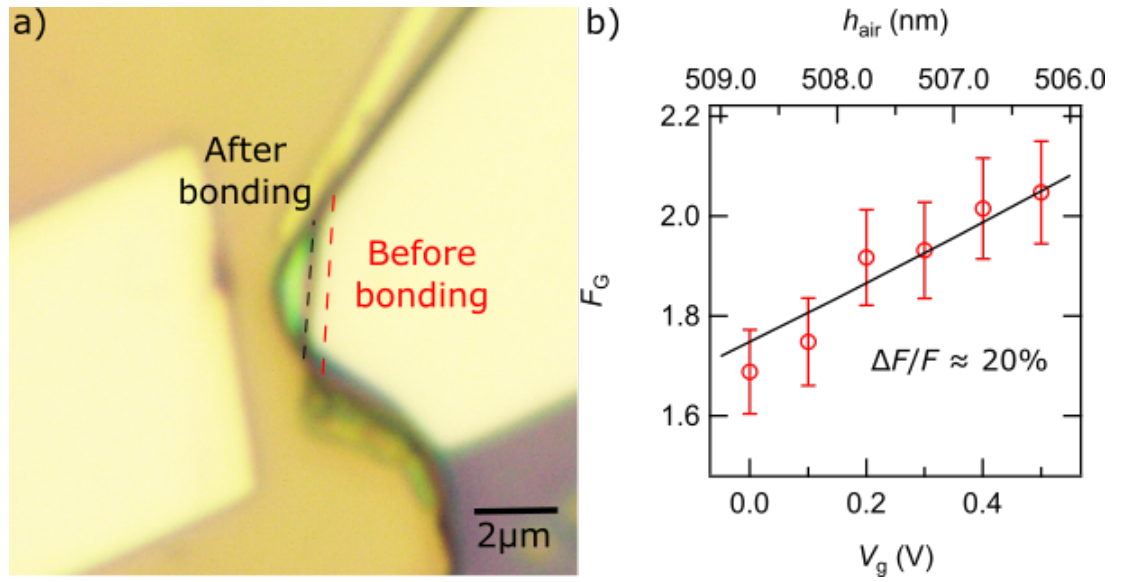


Figure 3.18: Raman factor data for Device WWA12 vs  $V_g$ . (a) Optical image of Device WWA12 after wirebonding, showing a significant change in cavity geometry. The change in BLG colour from yellow to green indicates a change in optical cavity height. (b) Modelled G peak Raman factor,  $F_G$ , (black) corresponding to optical cavity height (top) quantitatively agrees with our measured data (red circles), showing the tuning of  $F_G$  *in-situ* by 20%.

# Chapter 4

## Conclusions and Outlook

We have shown that when 2DMs, such as graphene, are incorporated in layered heterostructures, we can tune both the Raman factor ( $F$ ) and the light absorption ( $A$ ) that occur within them. With the addition of a highly reflective backplane mirror, such as Al, we were able to enhance and suppress these light-matter interactions by tuning the thickness of graphene optical cavities ( $h_{air}, h_{hBN}$ ). Moreover, we demonstrated that the Al mirror could be used to apply a gate voltage ( $V_g$ ) to a suspended BLG flake, thereby tuning the thickness of our optical cavity *in-situ*. This allows for Raman scattering and light absorption to be tuned *in-situ* in a single device. Our Raman factor and exclusive light absorption models predict that these interactions can be tuned further with the application of larger, but realizable voltages ( $V_g = 15$  V).

### 4.1 Main results

In Chapter 1, we gave context to this thesis based on recent results in the study of NOEMS and the fabrication of 2DM heterostructures. We reviewed the concepts of light absorption and Raman scattering in graphene, and presented an optical cavity design which would serve to tunably enhance/suppress these light-matter interactions. We also presented our models for light absorption and Raman factor, which use Fresnel equations to calculate these quantities for any 2DM heterostructure geometry. We showed that, according to our model, both light absorption and Raman scattering could be enhanced in BLG heterostructures.

In Chapter 2, we presented the all-dry, deterministic transfer technique which we developed to fabricate both supported and suspended optical cavities. This technique uses a nitrocellulose micro-stamp to pick-up and transfer 2DM into any-stacking-order heterostructures. We demonstrated through Raman spectroscopy that our transfer technique does not introduce significant defects or doping into the transferred 2D crystals. We then reviewed the process by which we convert raw Raman data (counts) into the Raman factor computed by our model. We found a quantitative agreement between Raman data and the theoretical Raman factor of a partially suspended BLG heterostructure (BLG/air/SiO<sub>2</sub>/Si), and also demonstrated that Raman factor and absorption can be tuned by 4 and 6 folds, respectively, as seen in Fig. 4.1(a-c).

In Chapter 3, we demonstrated that the addition of an Al backplane mirror increases the achievable Raman factors and exclusive light absorption.  $F_G$  could be tuned 19 folds across devices with varying spacer thickness ( $\Delta h_{hBN} \approx 75$  nm). We next presented the extra steps necessary for fabricating BLG/air/Al optical cavities (Fig. 4.1(d)), as well as the instrumentation and measurement/data analysis procedures that we use for precise Raman measurements. We found a quantitative agreement between Raman data and theoretical Raman factor for our BLG/air/Al optical cavity and demonstrated that we can tune  $F_G$  by 1.8 folds over a 10 nm change of cavity thickness in a single device, as seen in Fig. 4.1(e). According to our model, our measurements correspond to an exclusive light absorption of 15.6%, 3.4 times that of BLG in vacuum. Finally, we were able to electrostatically tune  $F_G$  by 1.2 folds and  $h_{air}$  by  $\approx 3$  nm with the application of 500 mV *in-situ*, as shown in Fig. 4.2(a). This proof of concept opens the door to further research at higher applied voltages, where we predict that Raman factor can be tuned by a factor of  $> 30000$  for  $\Delta V_g = 15$  V, as shown in Fig. 4.2(b).

## 4.2 Outlook

The near future of this project is to repeat our gate-tunable Raman factor measurements with higher  $V_g$  in order to demonstrate greater control of tunability in BLG/air/Al optical cavities. Our proof of concept and modelling (Fig. 4.2) allow us to believe that on/off ratios  $> 1000$  are achievable given the appropriate device geometry and by applying experimentally realizable  $V_g$ . In order to more closely

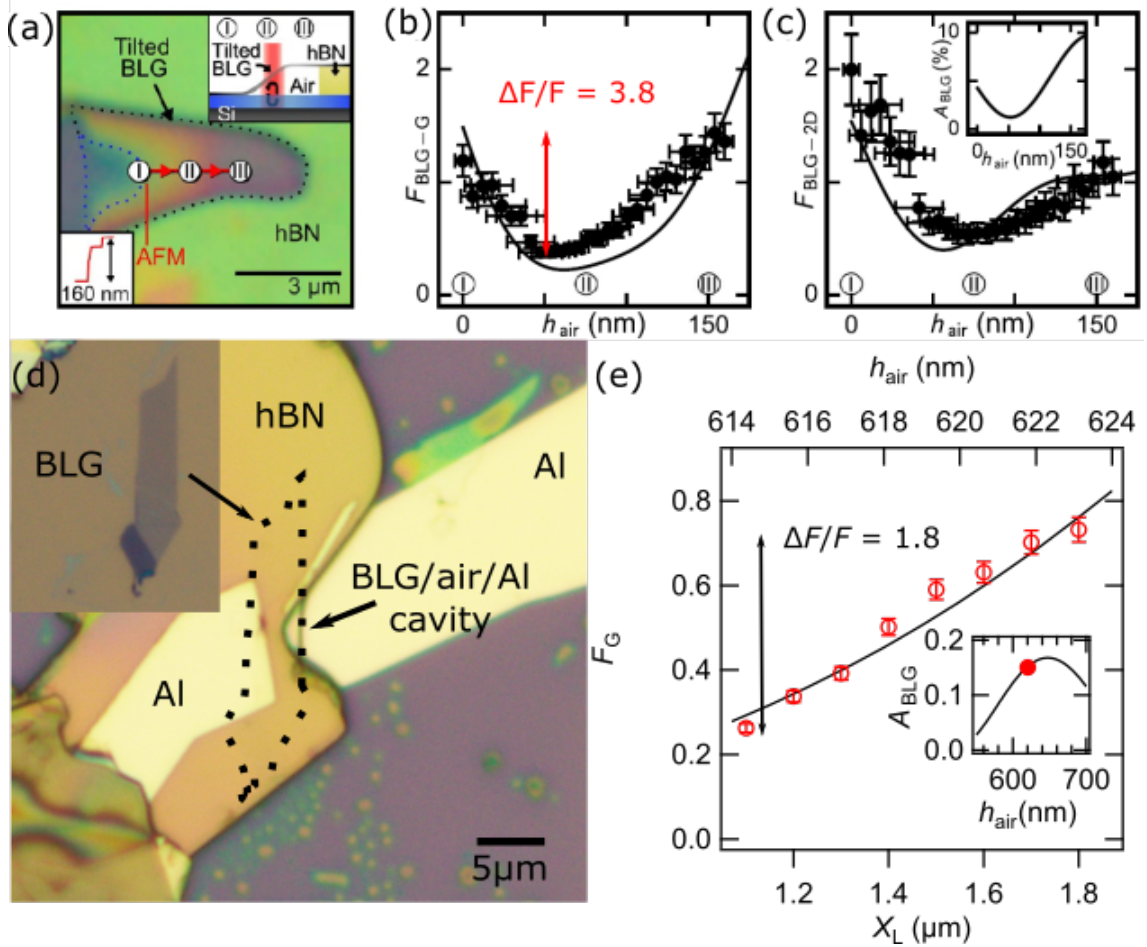


Figure 4.1: Tuning of BLG Raman scattering intensity and exclusive light absorption in suspended optical cavities. (a) Top optical view of a transferred tilted-suspended BLG flake. Region I is supported by SiO<sub>2</sub>, region II is suspended at heights ranging from 0 to 160 nm, and region III is at a constant height of 160 nm. The inset shows a cross-sectional view of the device's geometry. Raman factor as a function of air-spacer thickness ( $h_{air}$ ) for the G peak (b) and 2D peak (c). The inset shows the exclusive light absorption,  $A_{BLG}$ , for these same values of air-spacer thickness. (d) Top optical view of a BLG/air/Al optical cavity, where the BLG flake shown in the inset has been suspended over Al using a supporting hBN trench. (e) Modelled  $F_G$  (black) corresponding to optical cavity height (top) fitted to our averaged  $F_G$  data (red, bottom), showing the evolution of optical cavity height. The inset shows a modelled exclusive light absorption of 15.6% for our device.

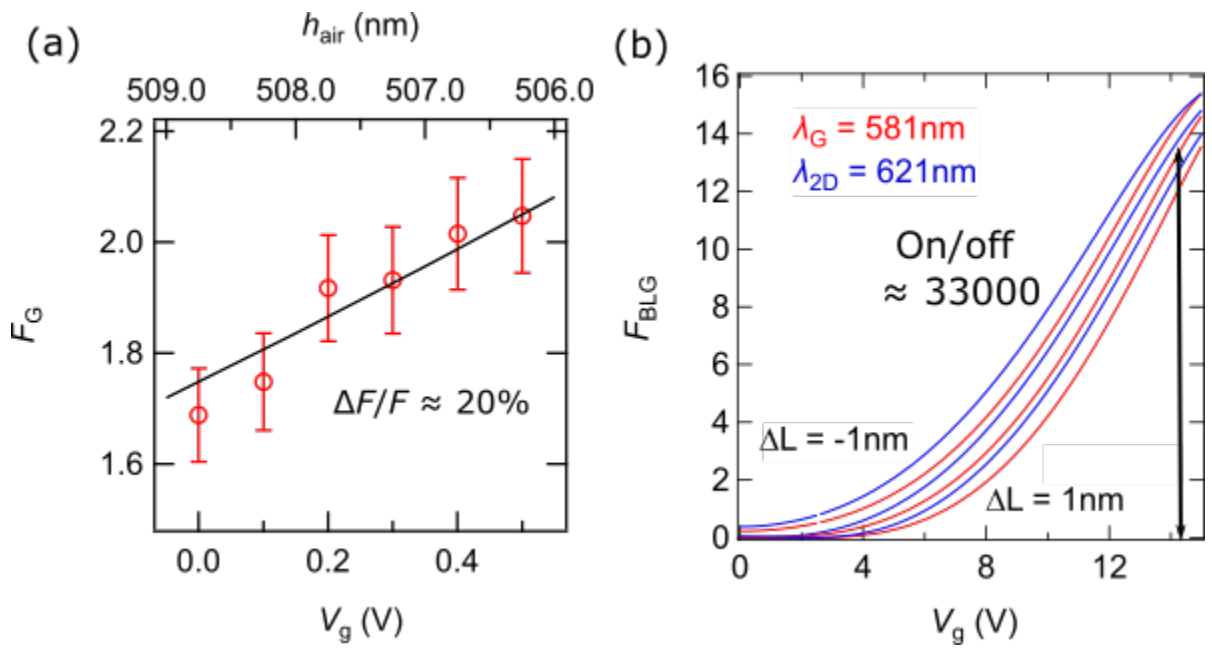


Figure 4.2: *In-situ* gate tunability of Raman scattering intensity. (a) Modelled G peak Raman factor,  $F_G$ , (black) corresponding to optical cavity thickness (top) quantitatively agrees with our measured data (red circles), showing the tuning of  $F_G$  *in-situ* by 20%. (b) Corresponding Raman factor ( $F_{\text{BLG}}$ ) model with increasing applied voltage predicting an increase from 0 to 15 for both the G peak (red) and 2D peak (blue) at 15 V and on/off ratios as high as 33000.

resemble our modelled gate-tunable Raman factor (beam geometry), we can fabricate our optical cavities over straight hBN trenches, as seen in Fig. 4.3(a), as opposed to the U-shaped trenches which we have used. Another possibility is to use our deterministic transfer technique to create our own trench using two straight-edged hBN flakes of similar thickness, as seen in Fig. 4.3(b,c). This technique would allow for the creation of an optical cavity with both the length and air-spacer thickness of our choosing.

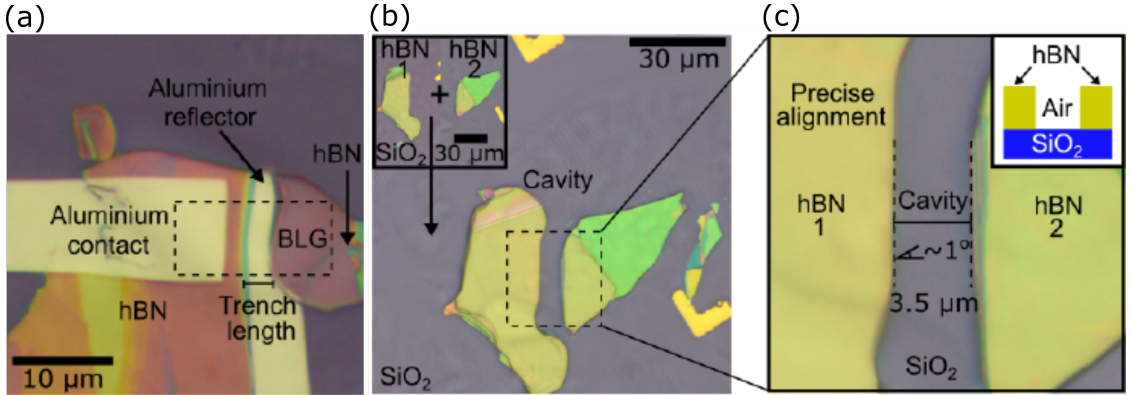


Figure 4.3: Fabrication of hBN trenches for beam-shaped optical cavities. (a) Top optical view of a beam-shaped hBN trench to be used to fabricate a BLG/air/Al optical cavity. (b) Two relatively large-area hBN crystals brought together by our deterministic transfer process to form a micro-cavity. Inset: hBN crystals on their former substrates. (c) Zoom in the cavity region, its length is  $3.5 \mu\text{m}$ . Inset: Schematic diagram of the cavity before Al deposition. Figures reproduced from [26].

There are several impactful applications which would benefit from *in-situ* tunability of Raman scattering intensity and exclusive light absorption. One such application is an optical transducer for light sensing, presented in Fig. 4.4(a). The addition of source/drain contacts to our existing optical cavity design would allow current to flow through the graphene. When exposed to light, a photo-current would be created in the graphene - the strength of which is controlled by the amount of light being absorbed. Our results demonstrate that we can tune the exclusive light absorption of graphene *in-situ*, thereby tuning the photo-current in such a device, with sizeable on/off ratios. Figure 4.4(b) presents an optical interferometric transducer, where the phase difference between light reflected from the top of the graphene and light reflected from the bottom of the cavity (constant phase element) can be used to reconstruct the movement of the graphene membrane [60].

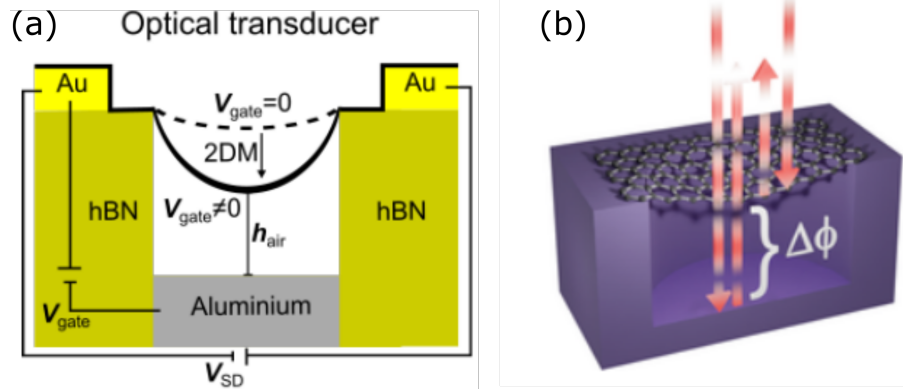


Figure 4.4: Application of tunable light absorption: optical transducer. (a) Schematic of an optical transducer, where the bottom gate contact deflects the graphene electrostatically and the source/drain contacts allow a current to flow across the graphene. Figure reproduced from [26]. (b) Interferometric optical interrogation, with interference from the light reflected at a suspended membrane and at the bottom of a cavity. Figure reproduced from [60].

# Bibliography

- [1] V. Singh, S. J. Bosman, B. H. Schneider, Y. M. Blanter, A. Castellanos-Gomez, and G. A. Steele. Optomechanical coupling between a multilayer graphene mechanical resonator and a superconducting microwave cavity. *Nature nanotechnology*, 9(10):820–824, 2014.
- [2] L. Midolo, A. Schliesser, and A. Fiore. Nano-opto-electro-mechanical systems. *Nat. Nanotechnol.*, 13(1):11–18, 2018.
- [3] Swapan K. Roy, Vincent T. K. Sauer, Jocelyn N. Westwood-Bachman, Anandram Venkatasubramanian, and Wayne K. Hiebert. Improving mechanical sensor performance through larger damping. *Science*, 360(6394):eaar5220, 2018.
- [4] R. Frisenda, E. Navarro-Moratalla, P. Gant, D. Pérez De Lara, P. Jarillo-Herrero, R. V. Gorbachev, and A. Castellanos-Gomez. Recent progress in the assembly of nanodevices and van der waals heterostructures by deterministic placement of 2d materials. *Chemical Society Reviews*, 47(1):53–68, 2018.
- [5] S. Fan, Q. A. Vu, M. D. Tran, S. Adhikari, and Y. H. Lee. Transfer assembly for two-dimensional van der waals heterostructures. *2D Mater.*, 7(2):022005, 2020.
- [6] K. S. Novoselov, A. Mishchenko, A. Carvalho, and A. H. Castro Neto. 2d materials and van der waals heterostructures. *Science*, 353(6298):aac9439, 2016.
- [7] Y. Liu, Y. Huang, and X. Duan. Van der waals integration before and beyond two-dimensional materials. *Nature*, 567(7748):323–333, 2019.
- [8] B. Li, J. Yin, X. Liu, H. Wu, J. Li, X. Li, and W. Guo. Probing van der waals interactions at two-dimensional heterointerfaces. *Nat. Nanotechnol.*, 14(6):567–572, 2019.

- [9] M. Yankowitz, Q. Ma, P. Jarillo-Herrero, and B. J. LeRoy. van der waals heterostructures combining graphene and hexagonal boron nitride. *Nature Reviews Physics*, 1(2):112–125, 2019.
- [10] J. C. W. Song and N. M. Gabor. Electron quantum metamaterials in van der waals heterostructures. *Nat. Nanotechnology*, 13(11):986–993, 2018.
- [11] P. Rivera, H. Yu, K. L. Seyler, N. P. Wilson, W. Yao, and X. Xu. Interlayer valley excitons in heterobilayers of transition metal dichalcogenides. *Nat. Nanotechnol.*, 13(11):1004–1015, 2018.
- [12] T. Deilmann, M. Rohlfing, and U. Wurstbauer. Light–matter interaction in van der waals hetero-structures. *Journal of Physics: Condensed Matter*, 32(33):333002, 2020.
- [13] M. Florian, M. Hartmann, A. Steinhoff, J. Klein, A. W. Holleitner, J. J. Finley, T. O. Wehling, M. Kaniber, and C. Gies. The dielectric impact of layer distances on exciton and trion binding energies in van der waals heterostructures. *Nano Lett.*, 18(4):2725–2732, 2018.
- [14] K. H. Kim, M. Yankowitz, B. Fallahazad, S. Kang, H. C. P. Movva, S. Huang, S. Larentis, C. M. Corbet, T. Taniguchi, K. Watanabe, S. K. Banerjee, B. J. LeRoy, and E. Tutuc. van der waals heterostructures with high accuracy rotational alignment. *Nano Lett.*, 16(3):1989–1995, 2016.
- [15] A. C. McRae, G. Wei, and A. R. Champagne. Graphene quantum strain transistors. *Physical Review Applied*, 11(5), 2019.
- [16] X. Zhang, K. Makles, L. Colombier, D. Metten, H. Majjad, P. Verlot, and S. Berciaud. Dynamically-enhanced strain in atomically thin resonators. *Nat Commun*, 11(1):1–9, 2020.
- [17] Y. Cao, V. Fatemi, S. Fang, K. Watanabe, T. Taniguchi, E. Kaxiras, and P. Jarillo-Herrero. Unconventional superconductivity in magic-angle graphene superlattices. *Nature*, 556(7699):43–50, 2018.

- [18] L. Xian, D. M. Kennes, N. Tancogne-Dejean, M. Altarelli, and A. Rubio. Multiflat bands and strong correlations in twisted bilayer boron nitride: Doping-induced correlated insulator and superconductor. *Nano Lett.*, 19(8):4934–4940, 2019.
- [19] H. Song, S. Jiang, D. Ji, X. Zeng, N. Zhang, K. Liu, C. Wang, Y. Xu, and Q. Gan. Nanocavity absorption enhancement for two-dimensional material monolayer systems. *Optics Express*, 23(6):7120–7130, 2015.
- [20] I. Epstein, B. Terrés, A. J. Chaves, V. Pusapati, D. A. Rhodes, B. Frank, V. Zimmermann, Y. Qin, K. Watanabe, T. Taniguchi, H. Giessen, S. Tongay, J. C. Hone, N. M. R. Peres, and F. H. L. Koppens. Near-unity light absorption in a monolayer ws<sub>2</sub> van der waals heterostructure cavity. *Nano Letters*, 20(5):3545–3552, 2020.
- [21] M. Casalino, U. Sassi, I. Goykhman, A. Eiden, E. Lidorikis, S. Milana, D. De Fazio, F. Tomarchio, M. Iodice, G. Coppola, and A. C. Ferrari. Vertically illuminated, resonant cavity enhanced, graphene–silicon schottky photodetectors. *ACS Nano*, 11(11):10955–10963, 2017.
- [22] B. J. Eggleton, C. G. Poulton, P. T. Rakich, M. J. Steel, and G. Bahl. Brillouin integrated photonics. *Nature Photonics*, 13(10):664–677, 2019.
- [23] C. Haffner, A. Joerg, M. Doderer, F. Mayor, D. Chelladurai, Y. Fedoryshyn, C. I. Roman, M. Mazur, M. Burla, H. J. Lezec, V. A. Aksyuk, and J. Leuthold. Nano–opto-electro-mechanical switches operated at cmos-level voltages. *Science*, 366(6467):860–864, 2019.
- [24] X. Zhang, C. De-Eknamkul, J. Gu, A. L. Boehmke, V. M. Menon, J. Khurgin, and E. Cubukcu. Guiding of visible photons at the ångström thickness limit. *Nat. Nanotechnol.*, 14(9):844–850, 2019.
- [25] I. G. Rebollo, F. C. Rodrigues-Machado, W. Wright, G. J. Melin, and A. R. Champagne. Thin-suspended 2d materials: facile, versatile, and deterministic transfer assembly. *2D Materials*, 8(3):035028, 2021.
- [26] I. G. Rebollo. *Thin-Suspended 2D Heterostructures: Deterministic Transfer and Tunable Graphene Light Absorption*. PhD thesis, 2020.

- [27] A. H. Castro Neto, F. Guinea, N. M. R. Peres, K. S. Novoselov, and A. K. Geim. The electronic properties of graphene. *Reviews of Modern Physics*, 81(1):109–162, 2009.
- [28] M. S. Dresselhaus, A. Jorio, and R. Saito. Characterizing graphene, graphite, and carbon nanotubes by raman spectroscopy. *Annual Review of Condensed Matter Physics*, 1(1):89–108, 2010.
- [29] R. R. Nair, P. Blake, A. N. Grigorenko, K. S. Novoselov, T. J. Booth, T. Stauber, N. M. R. Peres, and A. K. Geim. Fine structure constant defines visual transparency of graphene. *Science*, 320(5881):1308–1308, 2008.
- [30] I. Al-Naib, J. E. Sipe, and M. M. Dignam. High harmonic generation in undoped graphene: Interplay of inter-and intraband dynamics. *Physical Review B*, 90(24):245423, 2014.
- [31] Y. Guo, S. Jiang, X. Chen, M. Mattei, J. A. Dieringer, J. P. Ciraldo, and R. P. Van Duyne. Using a fabry–perot cavity to augment the enhancement factor for surface-enhanced raman spectroscopy and tip-enhanced raman spectroscopy. *The Journal of Physical Chemistry C*, 122(26):14865–14871, 2018.
- [32] A. C. Ferrari, J. C. Meyer, V. Scardaci, C. Casiraghi, M. Lazzeri, F. Mauri, S. Piscanec, D. Jiang, K. S. Novoselov, S. Roth, and A. K. Geim. Raman spectrum of graphene and graphene layers. *Phys. Rev. Lett.*, 97(18):187401, 2006.
- [33] A. C. Ferrari and D. M. Basko. Raman spectroscopy as a versatile tool for studying the properties of graphene. *Nat. Nanotechnology*, 8(4):235–246, 2013.
- [34] M. S. Dresselhaus and G. Dresselhaus. Intercalation compounds of graphite. *Advances in Physics*, 30(2):139–326, 1981.
- [35] L. M. Malard, M. A. Pimenta, G. Dresselhaus, and M. S. Dresselhaus. Raman spectroscopy in graphene. *Physics Reports*, 473(5-6):51–87, 2009.
- [36] G. Froehlicher and S. Berciaud. Raman spectroscopy of electrochemically gated graphene transistors: Geometrical capacitance, electron-phonon, electron-electron, and electron-defect scattering. *Phy. Rev. B*, 91(20):205413, 2015.

- [37] D. Graf, F. Molitor, K. Ensslin, C. Stampfer, A. Jungen, C. Hierold, and L. Wirtz. Spatially resolved raman spectroscopy of single- and few-layer graphene. *Nano Lett.*, 7(2):238–242, 2007.
- [38] R. J. Shiue, Y. Gao, C. Tan, C. Peng, J. Zheng, D. K. Efetov, Y. D. Kim, J. Hone, and D. Englund. Thermal radiation control from hot graphene electrons coupled to a photonic crystal nanocavity. *Nat. Commun.*, 10(1):109, 2019.
- [39] A. Reserbat-Plantey, S. Klyatskaya, V. Reita, L. Marty, O. Arcizet, M. Ruben, N. Bendiab, and V. Bouchiat. Time- and space-modulated raman signals in graphene-based optical cavities. *Journal of Optics*, 15(11):114010, 2013.
- [40] E. Hecht. *Optics* 4th ed. a. black, ed, 2002.
- [41] Y. Y. Wang, Z. H. Ni, Z. X. Shen, H. M. Wang, and Y. H. Wu. Interference enhancement of raman signal of graphene. *Applied Physics Letters*, 92(4):043121, 2008.
- [42] D. Metten, F. Federspiel, M. Romeo, and S. Berciaud. All-optical blister test of suspended graphene using micro-raman spectroscopy. *Physical Review Applied*, 2(5):054008, 2014.
- [43] D. Metten, G. Froehlicher, and S. Berciaud. Monitoring electrostatically-induced deflection, strain and doping in suspended graphene using raman spectroscopy. *2D Materials*, 4(1):014004, 2016.
- [44] D. Yoon, H. Moon, Y. W. Son, J. S. Choi, B. H. Park, Y. H. Cha, Y. D. Kim, and H. Cheong. Interference effect on raman spectrum of graphene on SiO<sub>2</sub>/Si. *Phys. Rev. B*, 80(12):125422, 2009.
- [45] Andre K Geim and Irina V Grigorieva. Van der waals heterostructures. *Nature*, 499(7459):419–425, 2013.
- [46] S. J. Yang, S. Choi, F. Ngome, K. J. Kim, S. Y. Choi, and C. J. Kim. All-dry transfer of graphene film by van der waals interactions. *Nano Letters*, 19:3590–3596, 2019.

- [47] P. Blake, E. W. Hill, A. H. Castro Neto, K. S. Novoselov, D. Jiang, R. Yang, T. J. Booth, and A. K. Geim. Making graphene visible. *Appl. Phys. Lett.*, 91(6):063124, 2007.
- [48] Yusai Wakafuji, Rai Moriya, Satoru Masubuchi, Kenji Watanabe, Takashi Taniguchi, and Tomoki Machida. 3d manipulation of 2d materials using microdome polymer. *Nano Lett.*, 20(4):2486–2492, 2020.
- [49] X. Ma, Q. Liu, D. Xu, Y. Zhu, S. J. Kim, Y. Cui, L. Zhong, and M. Liu. Capillary-force-assisted clean-stamp transfer of two-dimensional materials. *Nano Lett.*, 17(11):6961–6967, 2017.
- [50] Francesco Bonaccorso, Antonio Lombardo, Tawfique Hasan, Zhipei Sun, Luigi Colombo, and Andrea C Ferrari. Production and processing of graphene and 2d crystals. *Materials Today*, 15(12):564–589, 2012.
- [51] Andrew Collins McRae. *Graphene Quantum Strain Transistors and Two-in-One Carbon Nanotube Quantum Transistors*. PhD thesis, 2018.
- [52] F. C. Rodrigues-Machado. *Nano-optical cavities for tunable light absorption by graphene*. PhD thesis, 2019.
- [53] A. Castellanos-Gomez, M. Buscema, R. Molenaar, V. Singh, L. Janssen, H. S. J. Van Der Zant, and G. A. Steele. Deterministic transfer of two-dimensional materials by all-dry viscoelastic stamping. *2D Materials*, 1(1):011002, 2014.
- [54] L. Tao, H. Li, Y. Gao, Z. Chen, L. Wang, Y. Deng, J. Zhang, and J. B. Xu. Deterministic and etching-free transfer of large-scale 2d layered materials for constructing interlayer coupled van der waals heterostructures. *Advanced Materials Technologies*, 3(5):1700282, 2018.
- [55] R. A. Hemnani, J. P. Tischler, C. Carfano, R. Maiti, M. H. Tahersima, L. Bartels, R. Agarwal, and V. J. Sorger. 2d material printer: a deterministic cross contamination-free transfer method for atomically layered materials. *2D Materials*, 6(1):015006, 2018.
- [56] See-Hun Yang, Ron Naaman, Yossi Paltiel, and Stuart SP Parkin. Chiral spintronics. *Nature Reviews Physics*, 3(5):328–343, 2021.

- [57] J. B. Wu, M. L. Lin, X. Cong, H. N. Liu, and P. H. Tan. Raman spectroscopy of graphene-based materials and its applications in related devices. *Chemical Society Reviews*, 47(5):1822–1873, 2018.
- [58] Ki Seok Kim, Ki Hyun Kim, Yeonsig Nam, Jaeho Jeon, Soonmin Yim, Eric Singh, Jin Yong Lee, Sung Joo Lee, Yeon Sik Jung, and Geun Young Yeom. Atomic layer etching mechanism of mos2 for nanodevices. *ACS Applied Materials and Interfaces*, 9(13):11967–11976, 2017.
- [59] Abedin Nematpour, Nicola Lisi, Angela Piegari, Laura Lancellotti, Guohang Hu, and Maria Luisa Grilli. Experimental near infrared absorption enhancement of graphene layers in an optical resonant cavity. *Nanotechnol.*, 30(44):445201, 2019.
- [60] Alexandre F Carvalho, Bohdan Kulyk, António JS Fernandes, Elvira Fortunato, and Florinda M Costa. A review on the applications of graphene in mechanical transduction. *Advanced Materials*, 34(8):2101326, 2022.
- [61] I Lindseth, A Bardal, and R Spooren. Reflectance measurements of aluminium surfaces using integrating spheres. *Optics and Lasers in Engineering*, 32(5):419–435, 1999.
- [62] Gareth Melin. *Spatial Dependence of Photocurrent and Photogeneration Mechanisms in Graphene Field Effect Transistors*. PhD thesis, 2019.
- [63] Duhee Yoon, Hyerim Moon, Hyeonsik Cheong, Jin Sik Choi, Jung Ae Choi, and Bae Ho Park. Variations in the raman spectrum as a function of the number of graphene layers. *J. Korean Phys. Soc*, 55(3):1299–1303, 2009.
- [64] CL Wong, M Annamalai, ZQ Wang, and M Palaniapan. Characterization of nanomechanical graphene drum structures. *Journal of Micromechanics and Microengineering*, 20(11):115029, 2010.
- [65] Wenzhong Bao, Kevin Myhro, Zeng Zhao, Zhen Chen, Wanyoung Jang, Lei Jing, Feng Miao, Hang Zhang, Chris Dames, and Chun Ning Lau. In situ observation of electrostatic and thermal manipulation of suspended graphene membranes. *Nano letters*, 12(11):5470–5474, 2012.

- [66] Changyao Chen. *Graphene NanoElectroMechanical Resonators and Oscillators*.  
PhD thesis, 2013.